Exploration of UHS scalability by SPS approach: Multiphysics simulation, critical dimensions, mechanisms and properties

Flavie Lebas, Levent Karacasulu, Mattia Biesuz, Jérôme Lecourt, Christelle Bilot, Sylvain Marinel, Charles Manière

Exploration of UHS scalability by SPS approach: multiphysics simulation, critical dimensions, mechanisms and properties

Flavie Lebas[1]*, Levent Karacasulu[2], Mattia Biesuz[2], Jérôme Lecourt[1], Christelle Bilot[1], Sylvain Marinel[1], Charles Manière[1]*

[1] Université Caen Normandie, ENSICAEN, CNRS, Normandie Univ, CRISMAT UMR6508, F-14000 CAEN, France

[2]University of Trento, Department of Industrial Engineering, Via Sommarive 9, 38123 Trento, TN, Italy

* Corresponding authors: flavie.lebas@ensicaen.fr , charles.maniere@ensicaen.fr

Keywords

Ultrafast High-Temperature Sintering; Material Extrusion; Additive Manufacturing; Scalability; Pressureless Spark Plasma Sintering

Abstract

Ultrafast High-Temperature Sintering (UHS) enables near-instantaneous densification of ceramics but is limited by part size, wall thickness, and cracking due to thermal inhomogeneities. This work introduces a scalable UHS approach using a modified Spark Plasma Sintering (SPS) chamber with a large working volume (~113 cm^3) and precise control, enabling the sintering of complex ceramic parts up to 30 mm. Direct Ink Writing (DIW) is employed to shape and debind components efficiently while preserving UHS advantages. A parametric study identifies optimal heating rates and critical wall thicknesses (≤1 mm) to minimize thermal stress. Finite element simulations link thermal gradients to stress development, offering predictive capability for complex geometries. The results reveal that organic binder decomposition strongly affects grain growth and residual porosity under ultrafast heating. This work demonstrates the feasibility of industrially scalable UHS and provides key insights for microstructure control and simulation-guided process design.

Highlights

- Scalable UHS-SPS enables ultra-rapid sintering of complex ceramic parts.
- Ultrafast debinding is crucial, with control over carbo-thermal reduction.
- Multiphysics simulations highlight the importance of radiation exposure and design.
- A reliable model for ultrafast sintering has been developed.

Graphical Abstract

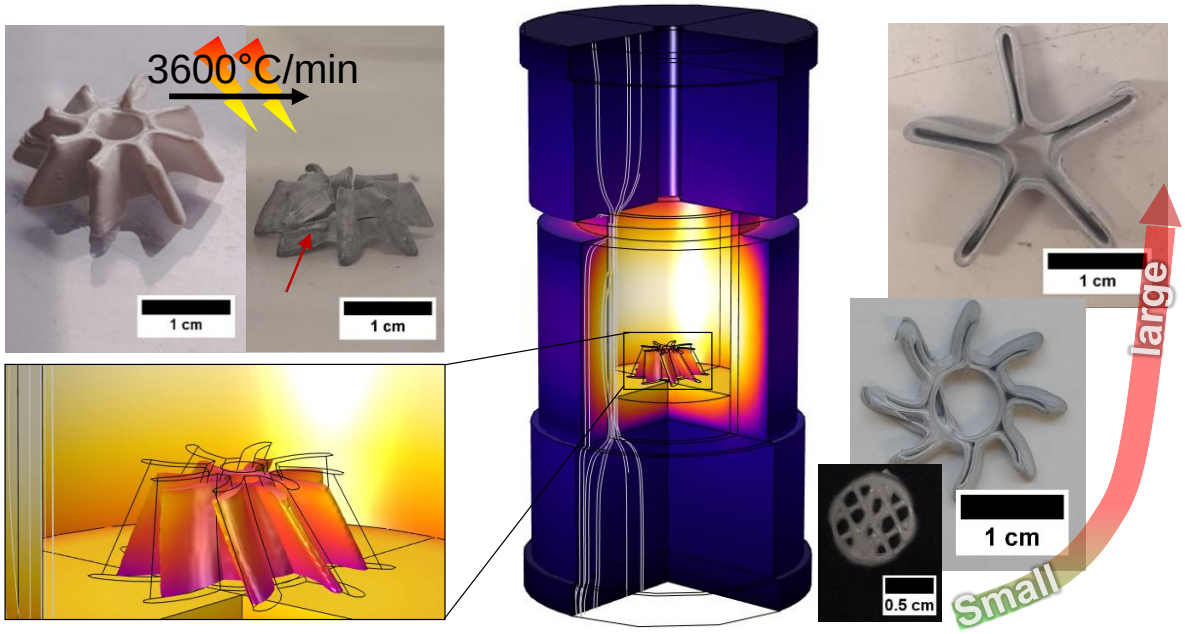

1. Introduction

Ultrafast high-temperature sintering is a very promising technology for the production of ceramic parts in mere seconds. In 2010, the flash sintering method renewed the interest in ultra-rapid sintering, which had been previously dominated by the fast-firing field [1]. Flash sintering (FS) studies have shown that many ceramics can be sintered in a few seconds if suitable electrical properties enable an abrupt current to flow across the material, accompanied by a temperature surge. Since then, numerous alternative methods have demonstrated that this ultrafast sintering behavior can be applied to other ceramics, provided that the heating is rapid and the temperature sufficiently high. Among these alternative approaches, we can cite black light sintering [2], fast firing [3–5], flash spark plasma sintering (pressure-assisted) [6,7], and flash microwave sintering [8,9]. Most FS studies have focused on small dog-bone-shaped samples without practical application, while some works have also investigated pellets or bar-shaped components [10]. In fact, the possibility of producing complex shapes and large samples by FS remains extremely limited, although some progress has been reported [11,12]. These limitations arise directly from the unstable nature of the flash phenomenon, in which a positive feedback loop is activated: a higher temperature induces a higher current, which in turn further increases the local temperature.

Recently, a technique similar to fast firing but operated at higher temperatures has emerged as particularly promising for ultrafast sintering of complex shapes [13]. This approach applies a heating surge to a temperature higher than in a conventional cycle by using graphite felt. This method is similar to fast firing because it involves ultrafast external heating applied directly to the specimen. In the original study [13], several complex shapes were produced without cracks and with a satisfactory microstructure. Since this study, which focused on reactive precursor (salt/oxide) and also on polymer-derived ceramics, the sintering-based method (called UHS) has been tested on numerous oxide-based powder materials [14–19], as well as carbides [20], and borides [21]. However, the size of specimens sintered by UHS remains small, with limited wall thickness. Attempts have been made to scale up the UHS process using a graphite powder bed as a conductive medium (P-UHS), and centimeter-scale complex shapes have been obtained [22].

In lower heating rate processes (~100°C/min), Pressureless Spark Plasma Sintering (P-SPS) [23] has been used to rapidly sinter metals [24,25], oxides [26,27], and carbides [28,29]. P-SPS is an interesting alternative, as it allows for rapid heating controlled by the SPS PID (proportional–integral–derivative) regulator. In 2022, Hofer *et al,* [30] showed that the P-SPS configuration can reach heating rates of up to 450 °C /min and is stable enough to sinter a large, intricate alumina impeller. In that study, the impeller was produced by vat photopolymerization, which requires a very long debinding phase. Nonetheless, this work

demonstrates that very rapid heating can be applied to a large, complex-shaped sample if it is thin enough to withstand thermal stresses. To overcome the issue of long debinding, coupling P-SPS with aqueous-based extrusion methods like DIW (Direct Ink Writing) is particularly promising. In such methods, the water can be evaporated, limiting the organic additive content to a few wt%, which can be rapidly debound [31,32]. The combination of DIW with P-SPS has been used for boron carbide [33] and, more recently, for barium titanate [34]. In the latter, DIW was also successfully combined with UHS. A similar coupling showed that fused filament fabrication (FDM) can also be used to produce gyroid zirconia ceramics [35], and it even demonstrated that partial debinding helps protect the sample from cracking during the UHS process.

Despite the interesting aspects of UHS, the challenge of scalability remains largely unresolved, as the process is still limited to small samples with thin walls [36]. Still, little is known about the relationship between the heating rate and the maximum wall thickness that can be processed without defects. Moreover, the 'traditional' UHS configuration is primarily heated from the upper and lower felt, which induces thermal gradients across different regions of the sample, particularly at the edges (near aperture) where convective heat losses are greater [35]. An improvement to the standard configuration was proposed by Zuo *et al*., who performed UHS in a graphite powder bed [22], however, this approach significantly increases the thermal mass of the heating element. In addition, their work employed a long thermal debinding cycle prior to UHS sintering.

Transitioning to real object fabrication by UHS requires addressing three main challenges: (i) the fabrication of a large demonstrator to heat large parts under UHS conditions, (ii) the identification of the critical heating rate to treat increasing wall thickness samples and (iii) the homogeneity of the UHS heating on highly complex geometries.

In this study, DIW was used to print alumina shapes with low organic content, varying in dimensions, geometry, and wall thickness. Different rapid debinding cycles were tested for each wall thickness to avoid undermining the advantages of UHS through excessively long debinding. The pressureless SPS concept was adapted to a large UHS working space into which the printed specimens could be inserted. The critical wall thickness/heating rate of printed tubes was tested under rapid (50 °C/min), ultra-rapid (1000 °C/min), and extreme UHS conditions (~3500 °C/min). Complex shapes were then tested using the fastest heating rate tolerated by each wall thickness. This study aims to provide stable heating and sintering conditions for the production of larger parts with thicker walls using UHS or ultra-rapid P-SPS.

2. Experiment and method

2.1. DIW formulations materials and printing

The direct ink writing (DIW) suspension was prepared in a single step using a planetary ball milling. The formulation comprised 47.0 vol% BMA15 alumina powder (specific surface area of 16.0 m^2/g, d_{50} = 0.12 µm, d_{100} = 0.40 µm, and a chemical purity of 99.99 %, Baikowski, France) 48.9 vol% water, and 4.04 vol% organic additives, which included 3.12 vol% of the dispersant dolapix CE64 (Zschimmer & Schwarz, Germany), 0.92 vol% carboxymethylcellulose (CMC, Sigma-Aldrich-Merck, Germany), and 0.48 vol% potassium hydroxide (KOH).

The TG/DSC analysis of the organic additives in argon atmosphere is presented in Figure 1. The dolapix CE64 decomposes up to 400 °C with two endothermic peaks. The decomposition of CMC is mainly concentrated between 250 °C and 350 °C, showing weakly exothermic peaks. The results reveal that both additives leave a carbon residue after pyrolysis. Dolapix CE64 shows a relatively low carbon residue of about 12 wt%, whereas CMC retains a significantly higher fraction (41 wt%). This higher residue in CMC is attributed to the presence of stable carbon chains, in particular aromatic cycles within the polymer structure, which favor carbon formation under inert atmosphere, leaving a black coloration on the pieces, as will be shown later. In summary, in the green bodies, the total volatile fraction (water and organics) amounted to ~53 vol%. TG/DSC analysis confirmed that the organic components decompose mainly between 250–400 °C, leaving limited carbon residues (≈12 wt% for Dolapix CE64 and ≈41 wt% for CMC). This quantification ensures a well-defined volatile content prior to sintering, which is critical for the UHS/UHS-SPS process

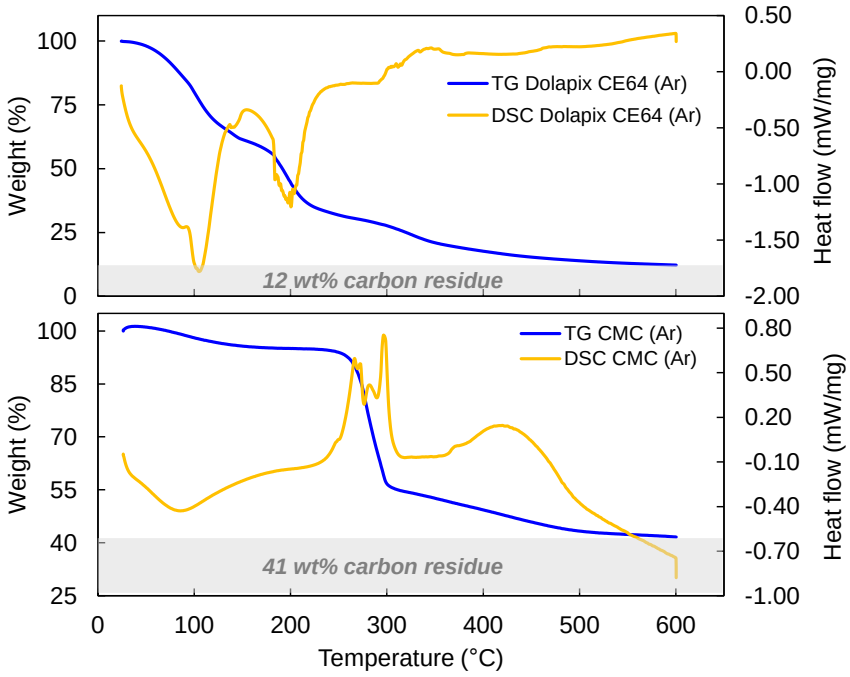

Figure 1: TG/DSC analysis of the organic additives: Dolapix CE64 and carboxymethylcellulose (CMC)

The addition of KOH to the DIW slurry formulation is intended to increase the pH of the suspension, creating a basic environment that stabilizes alumina in aqueous media [37]. This prevents particle agglomeration and ensures a homogeneous and stable slurry suitable for direct ink writing. The mixing was conducted using a Pulverisette 6 planetary mono mill grinder (Fritsch, Germany) for 1 hour and 45 minutes at a rotational speed of 350 rpm. Figure 2 presents the rheological properties of the formulated ink. The shear-thinning behavior, shown in red (viscosity as a function of the shear rate), is evidenced by a decrease in viscosity with increasing shear rate. This indicates that the ink flows more easily under higher shear, a desirable property for extrusion-based printing processes. In blue, the viscoelastic behavior is shown (complex moduli G′ and G″ as functions of oscillatory stress). The elastic component (G′) dominates the viscous component (G″), indicating a predominantly solid-like behavior. Notably, this solid-like nature remains stable under increasing oscillatory stress, confirming the presence of a broad Linear Viscoelastic Region (LVR). The transition from solid-like to liquid-like behavior, typically observed when G″ approaches or exceeds G′, is not seen here. However, a slight drop in modulus is observed near the rheometer's operational limit, suggesting that the ink does not exhibit a well-defined yield stress and maintains its solid-like behavior up to relatively high stress levels. Although the G′ and G″ profiles are not typical of conventional DIW inks, the use of CMC imparts a specific viscoelastic response that has

already proven effective for reproducible printing and shape retention, making the formulation suitable for this study [38].

After preparation, the suspension was carefully loaded into a syringe for printing. The printing process was carried out using an Eazao Bio (Eazao, China) robocasting printer equipped with a pneumatic dispensing system regulated by a manometer. The geometries of the printed parts were designed using FreeCAD software, and the printing strategy was configured in the Cura Ultimaker slicer. The paste was extruded through nozzles with diameters ranging from 0.4 mm to 0.8 mm at a printing speed of 20 mm/s. Consequently, bars and cylinders of 10 mm height with two different wall thicknesses namely 1.3 mm and 2.4 mm were printed, along with two distinct types of impeller models. Finally, small lattice structures were fabricated to compare the UHS process with the alternative UHS-SPS process.

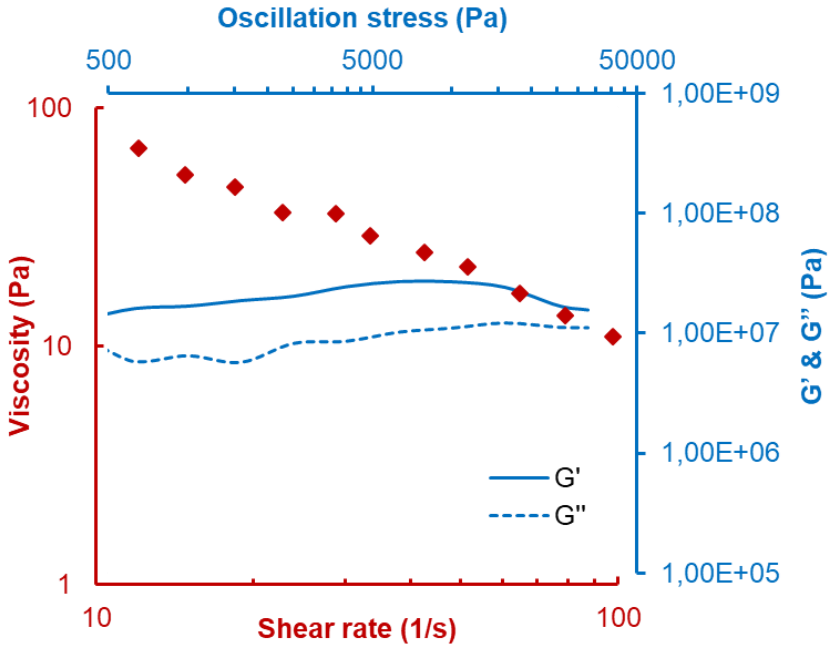

Figure 2: Rheological properties of the formulated ink: viscosity (red curve), the elastic component G' (blue curve), the viscous component G" (blue dashed curve).

2.2. Method

The objective of this study is to validate the capability of the UHS-SPS system to sinter larger parts compared to conventional UHS systems. This study is divided in five main steps.
(i) First, a comparison was conducted between the traditional UHS and our UHS-SPS systems using small lattice parts. The objective was to identify the potential differences between these two systems. Secondly, a parametric study was carried out to investigate the scalability of parts produced with the UHS-SPS system (Figure 3.a).
(ii) The next step consists of identifying the fastest crack-free P-SPS sintering conditions for thicknesses ranging from 1.3 mm called “thin” and 2.4 mm, “thick”. At this stage, the extreme UHS-SPS conditions are not yet applied. Instead, a rapid sintering profile with a 20 min dwell and varying heating rates is used. The explored heating rates ranged are from rapid (50°C/min) to ultra-rapid (1000°C/min) (Figure 3.b). The sintering temperature of this fast process must be higher than the conventional sintering temperature. It is set to 1600°C, as the conventional sintering temperature is close to 1400-1500°C for this powder [38]. The selected printed shapes are cylinders of 20 mm in diameter and 10 mm in height, with different wall thickness. The P-SPS uses the same configuration as the UHS-SPS. Temperature is measured by the top pyrometer, which is aimed directly inside the heated chamber. Since the pyrometer is calibrated for graphite, it is directed toward the inner support felt located inside the cylindrical hole. In this configuration, the surface of the felt responds quickly to heating while not being directly exposed to the radiation from the heating element. To compare the debinding impact, certain samples were debound in air at 600 °C using a fast heating and cooling rate of 10°C/min.
(iii) Once promising, thicknesses and heating rates are identified, extreme UHS-SPS conditions with a 3 min dwell time are tested on zigzag-shaped small lattices samples and then on complex shapes impeller to test the scalability of the UHS-SPS process (Figure 3.c).
(iv) Then, the samples with the most promising conditions were simulated by an electro-thermal-mechanical-microstructural simulation to assess the maximum developed thermal gradients and stress fields of each part. This helps relate the critical heating rate to a quantifiable temperature and stress field.
(v) Finally, the microstructure and mechanical properties are assessed.

a) UHS-conventional vs UHS-spark plasma sintering

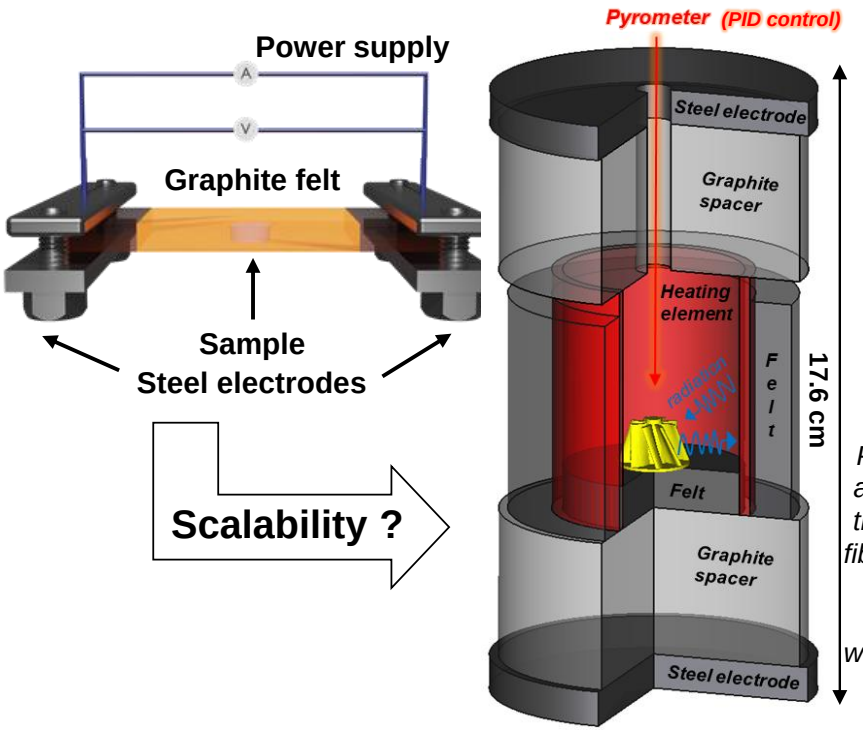

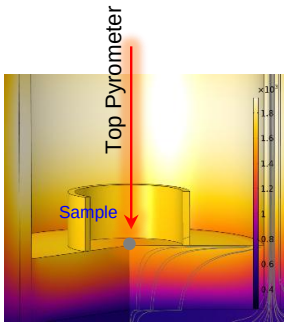

Pyrometer measurement at the felt surface '●' near the sample, the upper felt fibers are highly reactive to heating, making them perfectly suited to withstand ultra-fast heating

b) Critical heating rate explorations

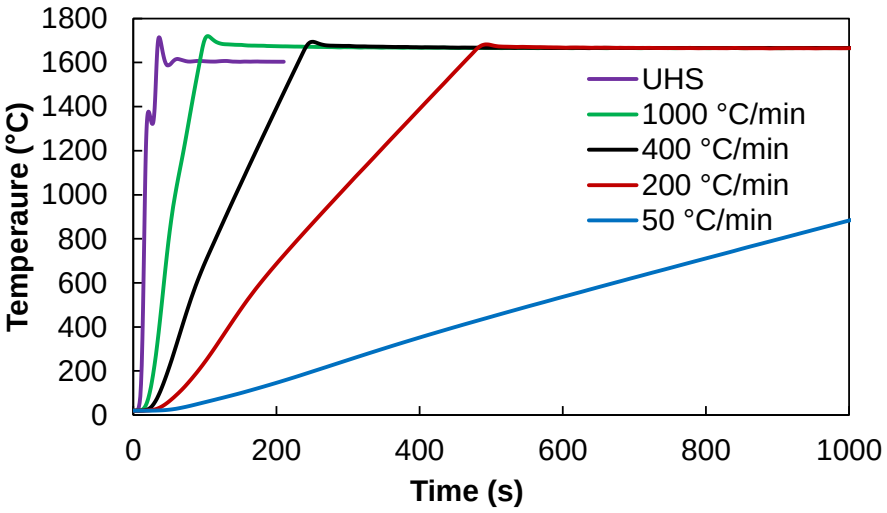

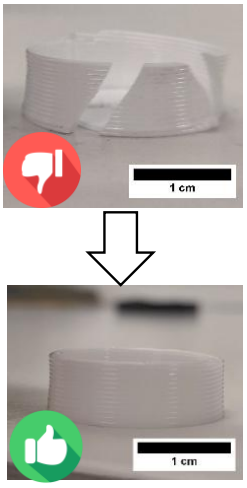

c) UHS-SPS : increasing shapes complexity explorations

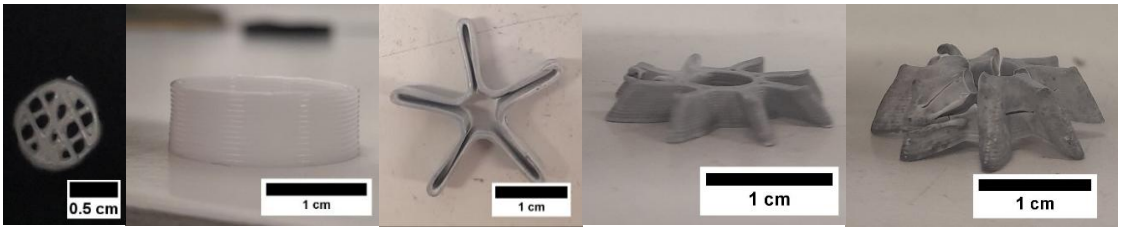

Figure 3: (a) Scheme of conventional UHS and UHS-SPS configurations exploration of (b) critical heating rate assessment study, (c) increasing shape complexity study.

2.3. Conventional UHS and UHS-SPS configurations and explorations

Conventional UHS experiments were conducted using a custom-built furnace in an argon atmosphere. A carbon felt (SGL Carbon Co., Germany) with dimensions of 24x70x6 mm^3 (nominally 5 mm, measured thickness ≈ 6 mm) was clamped between two steel electrodes, resulting in an electrode span (felt part distance between electrodes) of 30 mm with a cross-section of 24x6 mm^2 (Figure 3.a). The green complex-shaped bodies were inserted into the center of the carbon felt through a small hole, which was made using a spatula by piercing through from one side to the other. Before each experiment in an inert atmosphere (Ar), the chamber was evacuated twice to remove oxygen. An electric current was applied to the felt using a DC power supply (Agilent Technologies, model 6674A, Santa Clara, CA, USA), and the power source was always set to current control mode. Currents ranging from 32 A to 34 A were applied for 200 seconds.

The UHS-SPS prototype is designed to mimic the conventional UHS ultra-rapid heating response at a larger scale within SPS. Different strategies exist in the literature, like replacing the graphite felt with graphite powder [22] or bigger felt [39]. Here, we chose to replace the graphite felt of UHS configuration by a thin graphite cylindrical heating element (50x70x3) in red figure 3.a, which is externally thermally insulated, by a cylinder of graphite felt. The advantage of this configuration is that the heating element is reusable, highly responsive and resistant to thermal shock because it is 3 mm thick. This graphite element thickness was selected for its combination of reusability, thermal shock resistance, and performance, as it is generally considered too thin to withstand the applied contact pressure in SPS. To the best of our knowledge, has not been previously reported for pressureless UHS-SPS setups. The reduced thickness also makes the system more energy-efficient and more tolerant to small deformations. In addition, the temperature is PID-regulated directly in the chamber by a top pyrometer near the sample. Finally, this configuration enables a 113 cm^3 graphite chamber working space where large parts printed by DIW can be inserted. As seen in Figure 3.a, complex parts were centrally placed within the chamber and slightly shifted downward to lower the mid-chamber height, allowing thermal irradiation to occur both radial and coming from the upper part. This homogenizes the heating, favoring external and internal heating.

The exploration of critical heating rate and wall thickness was conducted as follows. All cylinders used in the ultra-rapid P-SPS explorations were subjected to a sintering cycle of 1600°C for 20 minutes with a heating rate of 200 °C /min. Based on the outcomes, such as the presence or absence of deformations or cracks, the heating rate was adjusted accordingly. For each set of conditions, a critical heating rate was identified (i.e., the maximum heating rate

without cracks). Finally, the optimal UHS-SPS conditions were tested on the different complex parts with different sizes.

2.4. Characterizations

The polished microstructures of the sintered parts were observed by SEM (JSM-7200F, JEOL, Japan). Energy Dispersive Spectroscopy (EDS) (X-Flash 6-60, Bruker, Germany) was used to map the chemical elements present. The hardness was characterized by Vickers micro-indentation (MMT-X7B, Matsuzawa, Japan) using a 1 kgf load. Approximately nine hardness measurements were taken at the core of the parts for each sintering temperature. The grain sizes of the various parts were measured by image analysis using open-source image processing software (Image J - National Institute of Mental Health, USA). The average grain size was assessed using the linear intercept method with a stereological factor of 1.56 [40]. The crystalline phases present in the sintered parts were analyzed by X-ray diffraction (D8 Advance Vario 1, Bruker), using Cu Kα (λ = 1.5406 Å) with a Johansson-type Ge(111) monochromator and a LynxEye detector. The measurement parameters were set to a 2θ range of 10° to 90°, with an angular step of 0.01°. The crystalline phases were identified by comparing the diffractograms with those reported in the X'Pert HighScore Plus software database.

2.5. FEM ETMM simulation of UHS_SPS

The Finite Element Method (FEM) simulations were conducted on the software COMSOL Multiphysics® using the heat transfer module to implement the Joule heating of the graphite parts and the surface-to-surface thermal radiation of the inner and outer surfaces. This electro-thermal model (ET) is coupled with a sintering model including the mechanical aspects of densification and grain growth. This sintering approach is then classified as mechanical or microstructural (MM). The whole simulation, coupling the heating (ET) and sintering (MM), is called "ETMM". The electro-thermal properties of the Mersen® 2333 graphite grade used for the spacer and the heating element have been uses in numerous spark plasma sintering simulations they can be found in ref [41]. The graphite felt used to confine the heating in the P-SPS prototype uses the thermal properties detailed in the UHS simulation in ref [35]. For the conventional UHS test, it was used to compare the UHS-SPS microstructures. The same experimental and simulation conditions of ref [35] were used. The simulated temperature curves were obtained by simulating the UHS test heating. The electro-thermal equations, boundary conditions, and key thermal and physical parameters of the materials and heating elements are provided in the Appendix.

From the simulated temperatures of the sample, the sintering model is simulated the densification and grain growth. The Skorohod-Olevsky model [42] is described in the appendix section with the identification equations. The conventional sintering model was first identified; subsequently, this model parameter was corrected to better reproduce the ultra-fast and UHS-SPS sintering behavior, which is modified by carbon contamination and the high heating rate.

3. Results and discussions

3.1. Conventional UHS vs SPS UHS on small specimen

To scale up the UHS process, a UHS-like SPS configuration has been developed. However, it is important to make sure the thermal history of this large volume configuration behaves similarly to conventional UHS. Consequently, both configurations were tested on 10 mm lattice printed samples. These specimens can be easily inserted into the felt aperture of the conventional UHS. As it was demonstrated experimentally [35] and confirmed later in this study, undebound specimens are preferred as they are less sensitive to cracks. This can primarily be attributed to the endothermic nature of binder decomposition in an inert atmosphere, which acts as a negative feedback on temperature and thus makes the temperature distribution more homogeneous. These preliminary tests then used undebound printed specimens. In the UHS-SPS configuration, heating is controlled by a PID system using a pyrometer aimed at the felt a few mm near to the sample. The choice of this pyrometer spot is motivated by the high heating responsiveness of the inner felt surfaces exposed to furnace radiation. Since this particular test involves a small grid, the spot may also overlap with the alumina grid; however, the emissivities of alumina and graphite are similar. Moreover, because the alumina sample is very thin, its heating response is also rapid. A dwell at 1600 °C is programmed for 200 seconds. As conventional UHS is monitored by imposed current, we explored 32 to 34 A during 200 s, as our calibrated simulation of the same conventional UHS configuration indicates this range corresponds to 1600°C [35].

The obtained results are reported in Figure 4.a. All sintered materials exhibited well-densified microstructures, with densities generally exceeding 98% of the theoretical value. When increasing the conventional UHS current, there is an obvious grain coarsening resulting from a higher sintering temperature. In general, the sample sintered under 32 A possesses the microstructure closest to the UHS-SPS (Figure 4.b), both in terms of relative density and grain size. Further increasing the UHS current causes grain growth but also a loss in terms of density, which is very clear at 34 A. Actually, this could be explained in terms of the carbo-thermal decomposition of alumina, resulting in the formation of new pores [43]. In the latter, evidence of carbon contamination and the appearance of porosity under high current were reported. Here, the same type of defect occurs, exhibiting a similar microstructure. The density

evolution is mimicked by the mechanical properties like hardness. One can, for instance, notice that when increasing the conventional UHS current, the density loss is coupled with a decrease of the microhardness. Furthermore, we can spot that besides conventional 32 A UHS samples possessing a density larger than UHS-SPS, their hardness is slightly lower, probably as a result of a coarser microstructure.

It is interesting to note that the UHS-SPS sample is not cracked, while conventional UHS shows a broken part on the edge because the 10 mm sample corresponds to the critical size limit of this configuration. It suggests the large SPS chamber provides a more homogeneous irradiation to the sample, which is encouraging for producing larger and complex parts. This could also be explained also considering the perfect axial symmetry of the SPS heating element compared with the conventional UHS. Actually, in conventional UHS, the sample is introduced through a hole present on the lateral side of the felt itself. This facilitates the radiative heat losses on the region of the sample facing the hole thus introducing thermal gradients. In addition, PID control results in a slightly lower heating rate compared to the abrupt application of a high current. However, the appearance of cracks at the edges supports the explanation of configuration heterogeneity.

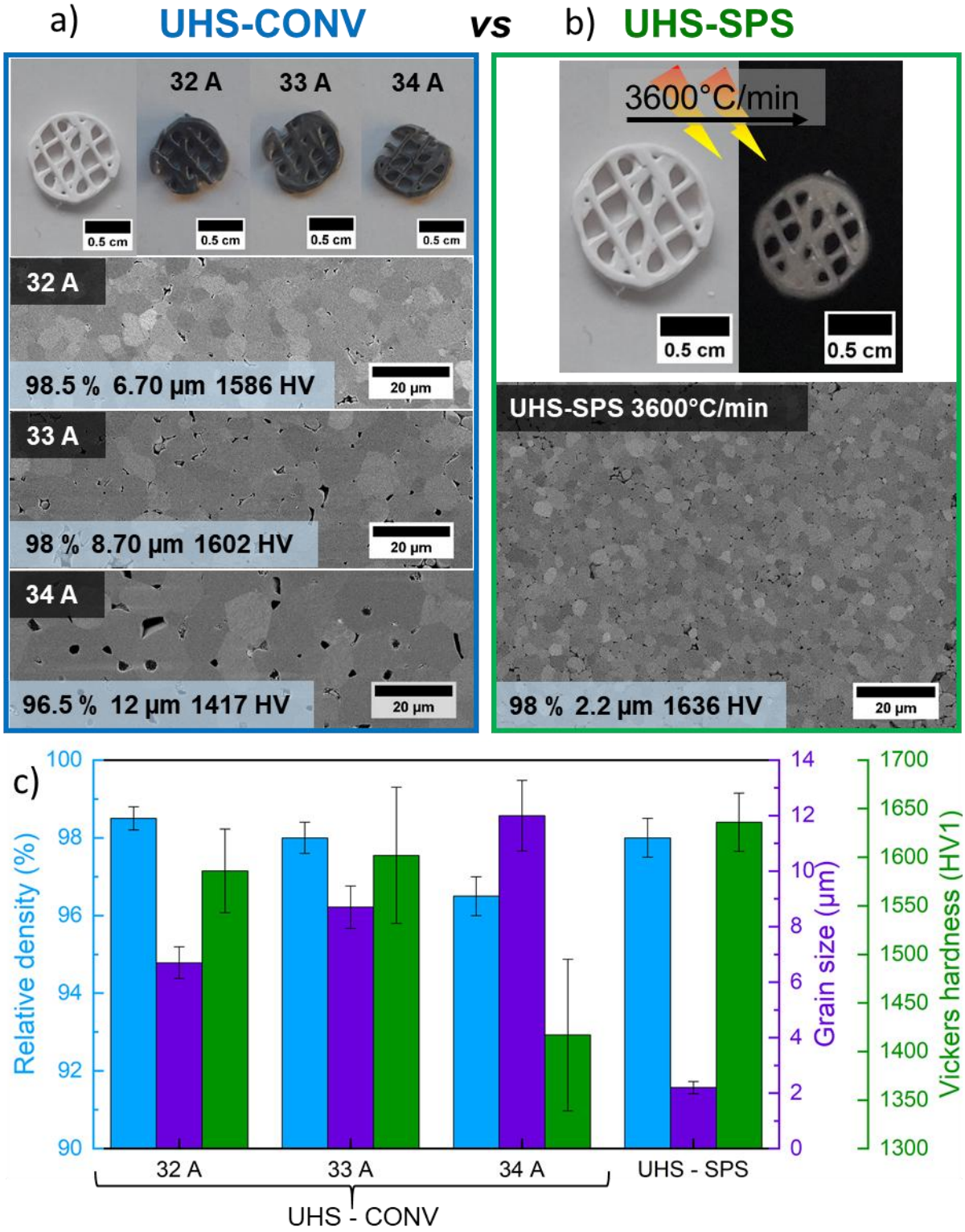

Figure 4. (a) Conventional UHS (based on graphite felts) for 32-34 A compared to (b) UHS-SPS (3600°C/min) at 1600°C, The main ceramic characteristics are compared in a histogram (c).

3.2. From rapid to ultra-rapid pressureless SPS

This section is dedicated to exploring the sintering behavior of larger samples, their brittle nature, modeling parameters, and microstructural characteristics under rapid to ultra-rapid heating conditions. Based on these observations, the most favorable UHS conditions identified here will be used for further optimization and analysis in ongoing work.

3.2.1. Stability zones

To successfully sinter large and complex parts using our UHS-SPS configuration, it is crucial to determine the critical wall thickness and heating rate. Large printed tubes are tested, as this geometry presents a moderate level of difficulty and offers a representative radiation exposure that differs between the inner and outer surfaces. These parameters have been analyzed and summarized in figure 5. The table presents the sintering outcome (defect-free or cracked) of tubes with a 20 mm diameter and 10 mm height as a function of their debinding condition (debound or undebound), wall thickness (thin or thick), and applied heating rate.

First, we observed that slightly thicker walls significantly reduce the maximum achievable heating rate. The highest heating rate recorded was 200°C/min for thick-walled samples, whereas thin-walled samples could withstand heating rates up to 1000°C/min. This limitation in thick-walled samples is likely due to increased thermal gradients and internal stresses.

Second, debound samples exhibited cracking at lower heating rates compared to undebound samples, regardless of wall thickness. This can be attributed to the nature of the consolidation process. The debinding at 600°C involves particles neck formation by surface diffusion consolidation. This interconnected porous network is a very brittle structure compared to loose powder. For the undebound case, the absence of heat treatment and the presence of organic binder is a more resistant structure to thermal shock. In addition, the *in situ* decomposition of the binders can delay the surface diffusion to higher temperature under ultra-fast heating condition, which shifts the brittle behavior to higher temperatures. To conclude, our findings suggest that it may be possible to sinter large and complex undebound parts under UHS conditions. Further investigations will be necessary to confirm these results for complex shapes and for extreme UHS conditions.

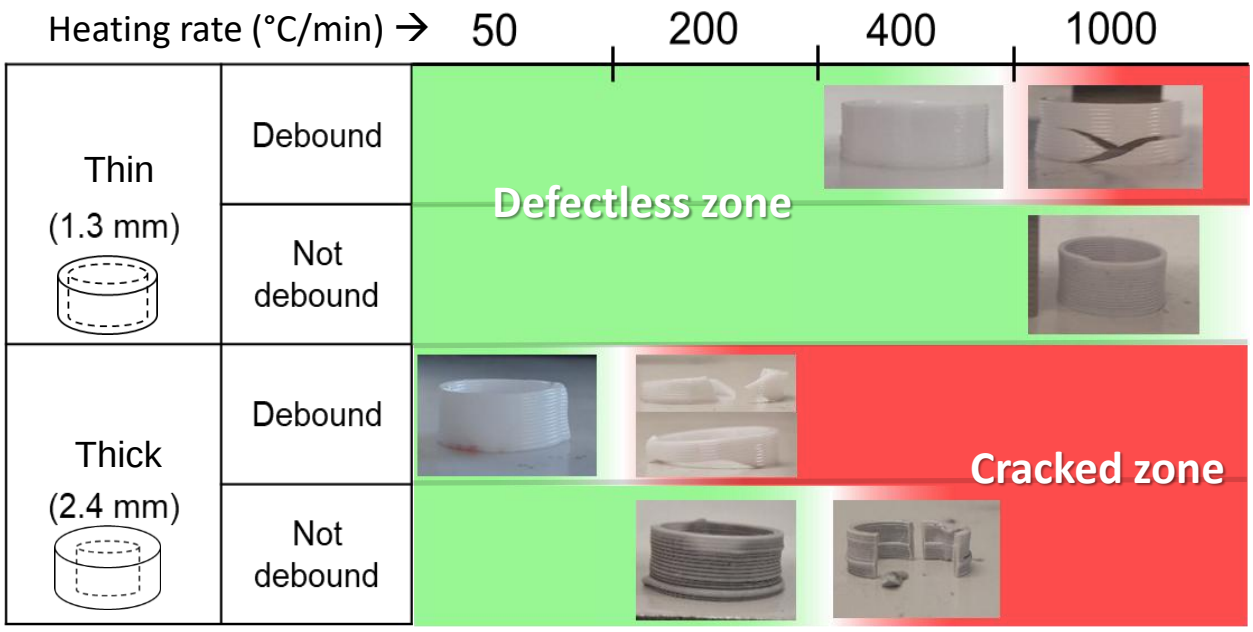

Figure 5. Determination of critical heating rate depending on the debinding method and the thickness of tube shape samples.

3.2.2. Microstructural characterization

The SEM images of parts produced at 400 °C/min are reported in Figure 6.a for the debound and undebound cases. This clearly points out that debinding at 600°C in air favors a clean and fully dense microstructure. The undebound case exhibits 3.6% of dark zones that are porosity and carbon traces, as it will be characterized later. This porosity can be related to the carbo-thermal reduction in UHS [43]. The other difference is the grain size, which is significantly larger for the undebound case, which implies a decrease in hardness. This effect seems to favor coarsening rather than densification.

The SEM microstructures of the parts sintered at their critical heating rates (crackfree) are shown in Figure 6.b along with the histogram of their main properties. The same phenomenon of porosity and larger grains is present between the debound and undebound cases. For the debound cases where the grain growth is slow, there is almost no difference in microstructure and hardness between the 50 and 400°C/min. For the undebound case, where the grain growth is faster, the 1000°C/min case has less sintering time, and lower densification and grain size than the 200°C/min case. This indicates that debound powders are less sensitive to the rapid cycle differences while undebound can exhibit clear microstructure differences. The undebound samples have gray appearance and are clearly polluted by carbon originating from the decomposition of the organic additives used for the 3D printing (see figure 1). There are two main origins to explain this higher coarsening impact for the

undebound case. It can be an effect of the carbon contamination, itself causing second-phase segregation and grain growth pinning, or a reduction effect which disturbs the diffusion by vacancy concentration disturbance. The last effect is coherent with the skin effect reported in Figure 6.c. In the latter, both debound and undebound samples (whether single or double–thickness) present significantly larger grain size near the surfaces in contact with the vacuum of the SPS chamber. It is well known the vacuum can cause reduction of oxide at high temperatures [44] and the grain aspects in the skin look like the microstructure coarsening in the undebound sample (except for the porosity, which is carbon originated). This observation suggests the carbon contamination implies a carbo-thermal reduction at high temperatures, and this reduction causes significant grain coarsening in the core of the undebound samples. It is known that a reducing atmosphere can accelerate coarsening over densification [45]. Mechanisms of non-equilibrium grain boundaries have recently been discussed as accelerating mechanism [46] that could also be impacted by carbon contamination. It is also worth noting that the rapid grain growth is not associated with pore detachment, suggesting that these large pores (where carbon appears to be present) have a high migration rate.

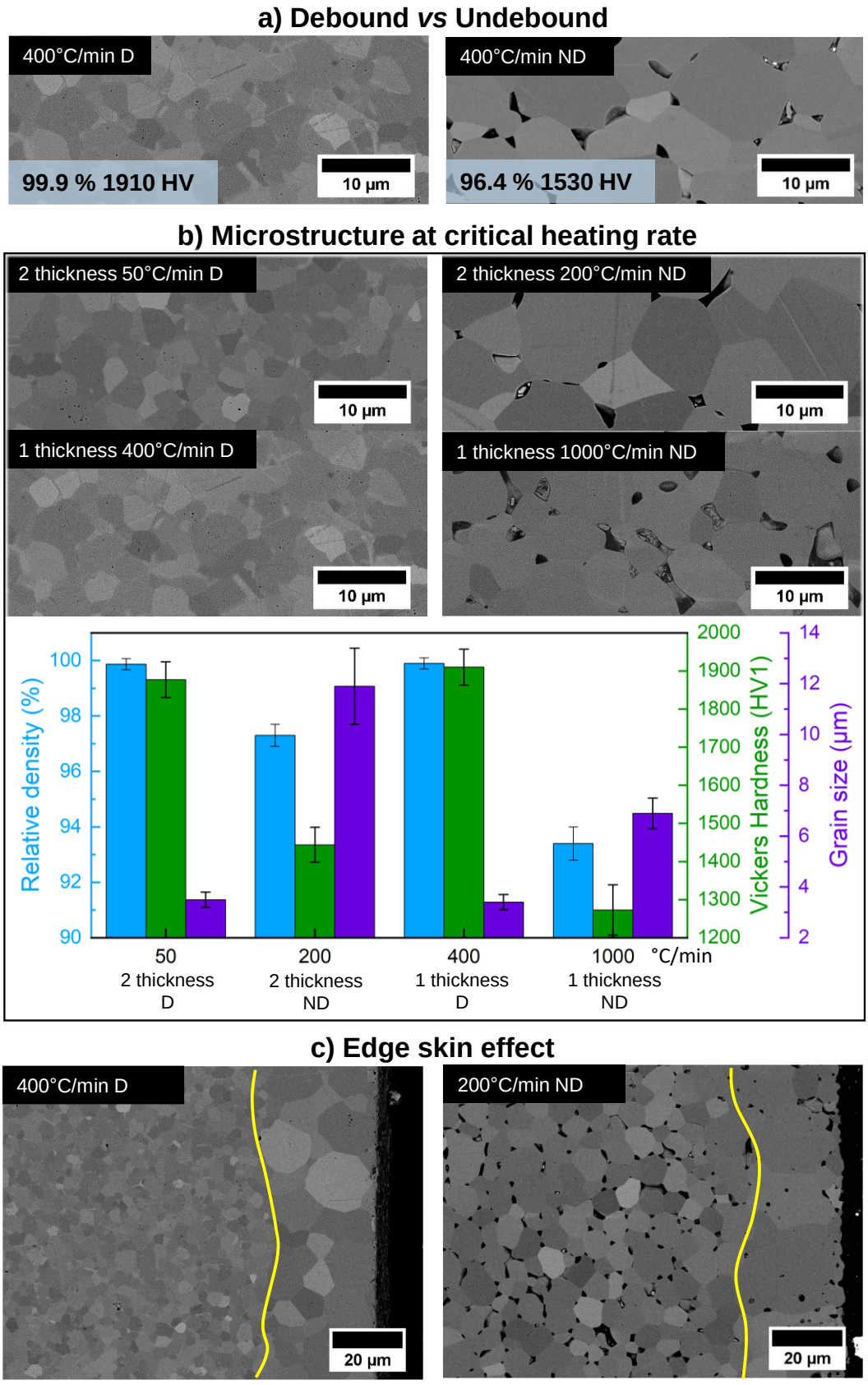

Figure 6. SEM microstructures: (a) microstructure comparison between debound and undebound parts, (b) microstructure and properties comparison at critical heating rate and (c) edge skin effect.

3.2.3. EDS and XRD analysis

In the undebound samples, the presence of residual carbon can potentially lead to the formation of graphite or carbide phases. To investigate this possibility, the microstructure of an undebound sample sintered at a heating rate of 1000 °C/min was analyzed using EDS mapping, as shown in Figure 7.a. As expected, both oxygen and aluminum were detected, indicating the presence of intergranular porosity. However, the most notable observation is the presence of carbon-rich regions near large pores. Carbon is also detected within some closed grains. At this stage, it is not possible to determine whether these carbon-rich zones consist of elemental carbon or carbide phases. Some regions appear to be graphite, particularly when isolated within pores. In contrast, other areas where carbon and aluminum coexist were further examined by XRD phase identification.

Figure 7.b presents the XRD results, which do not reveal any carbon-related phases such as graphite or carbides. Only α-alumina was identified. This suggests that the carbon-rich regions are of low volume fraction and fall below the detection threshold of XRD. The results indicate that carbon contamination is limited, likely due to the carbo-thermal reduction effects occurring during sintering. Following the sintering step, which was performed under vacuum, only trace amounts of carbon remain near large pores.

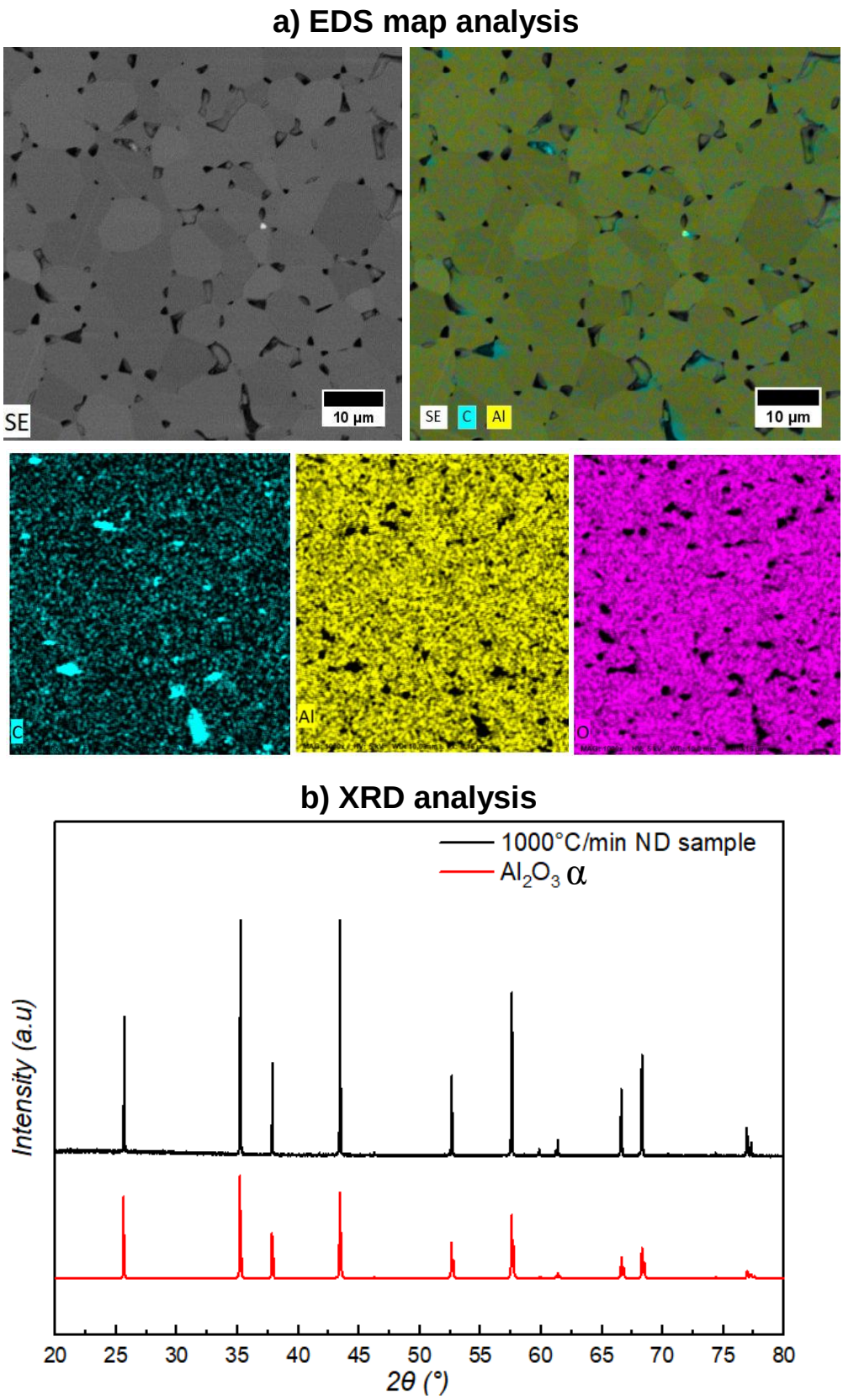

Figure 7: Carbon contamination analyses, (a) EDS map, (b) XRD of the powder and undebound sintered specimen at 1000°C/min.

3.2.4. Ultra-rapid sintering model assessment

The conventional sintering model is first assessed by dilatometry on the printed debound specimen. As the sintering is performed on graphite support and in vacuum, the sintering dilatometry is conducted in similar conditions using graphite support and an inert atmosphere (Ar) instead of vacuum. The analysis of the conventional dilatometry is reported in figure 8.a. The first graph indicates isotropic sintering as the linear shrinkage in the building direction (axis z) and in the radial direction (axis r) are strictly identical. Based on this, the porosity curve is calculated. Using the experimental sintering bulk modulus (ψ) of BMA15 alumina [47], it is possible to use directly the regression equation (12) to assess the activation energy Q and pre-exponent viscosity constant η_0. An activation energy of 482 kJ/mol is found which aligns well with the expected value for alumina [48]. Then, the grain size curves are predicted by equation (16) and using the already identified parameters (η_0, Q, ψ), the Skorohod's sintering stress expression (P_l) [42] and the final stage porosity curve. The two grain size curves are reported in Figure 8.a. As these curves accuracy strongly depends on the final stage sintering curve densification, the end of the curve is often very noisy as the densification is very low at the end. However, analyzing the trend of the curve with the final grain size measured, an m=2 (lattice diffusion mechanism) is clearly more suited for this powder. As this predicted curve is very noisy, it is modeled by a grain growth model that reproduces a similar grain size curve. This grain growth model is adjusted to the pressureless sintering and P-SPS conditions from an SPS grain growth model of the same powder with the fixed values of Qg=200 kJ/mol, p=2 [49]. The k_0 constant (initially of 1E-16 m^3/s for SPS) is modified to fit the grain size curve. As the grain size curve is not very logarithmic in porosity zone, a porosity function [50,51] is used to better adjust the model to the expected grain growth curve. The parameters of this grain growth model are reported in Table 1 with in green the grain size curve in figure 5.a. The final densification model reported in figure 8.b shows the experimental porosity curve is well reproduced by the model with grain growth (green curve) while the model without grain growth (black curve) does not reproduce the final stage porosities.

This conventional sintering behavior does not perfectly reproduce the ultra-rapid sintering behavior of the debound (400 °C/min) and undebound (1000 °C/min) sample as can be seen in figure 8.b (dashed curves). The ceramic has mutual porosity and grain growth. For the undebound specimens, significant carbon contamination disturbs the grain growth [52,53] and which in turn disturbs the densification. The adjusted parameters require a careful adjustment of the grain growth porosity dependence and of the grain size sensitivity (m) which is 2 for conventional, reduced 1.5 for deboud 400 °C/min and 1 for undebound 1000 °C/min.

The model has then been modified to better reproduce these ultra-rapid conditions

(continuous curves, see Figure 8). For UHS-SPS the effect of densification limitation is less present and the model was also adjusted. The modified grain growth parameters are summarized in Table 1. The grain growth is highly sensitive the carbo-thermal reduction and the model needs to be adjusted for each heating rate and debinding conditions.

Table 1 Grain growth model parameters for the conventional and ultra-rapid sintering.

Parameter	Conventional model	Dedound model 400°C/min	Undeboud model 1000°C/min	Undebound UHS-SPS 3600°C/min
n	3	3	3	6
θ_c	0.05	0.05	0.02	0.002

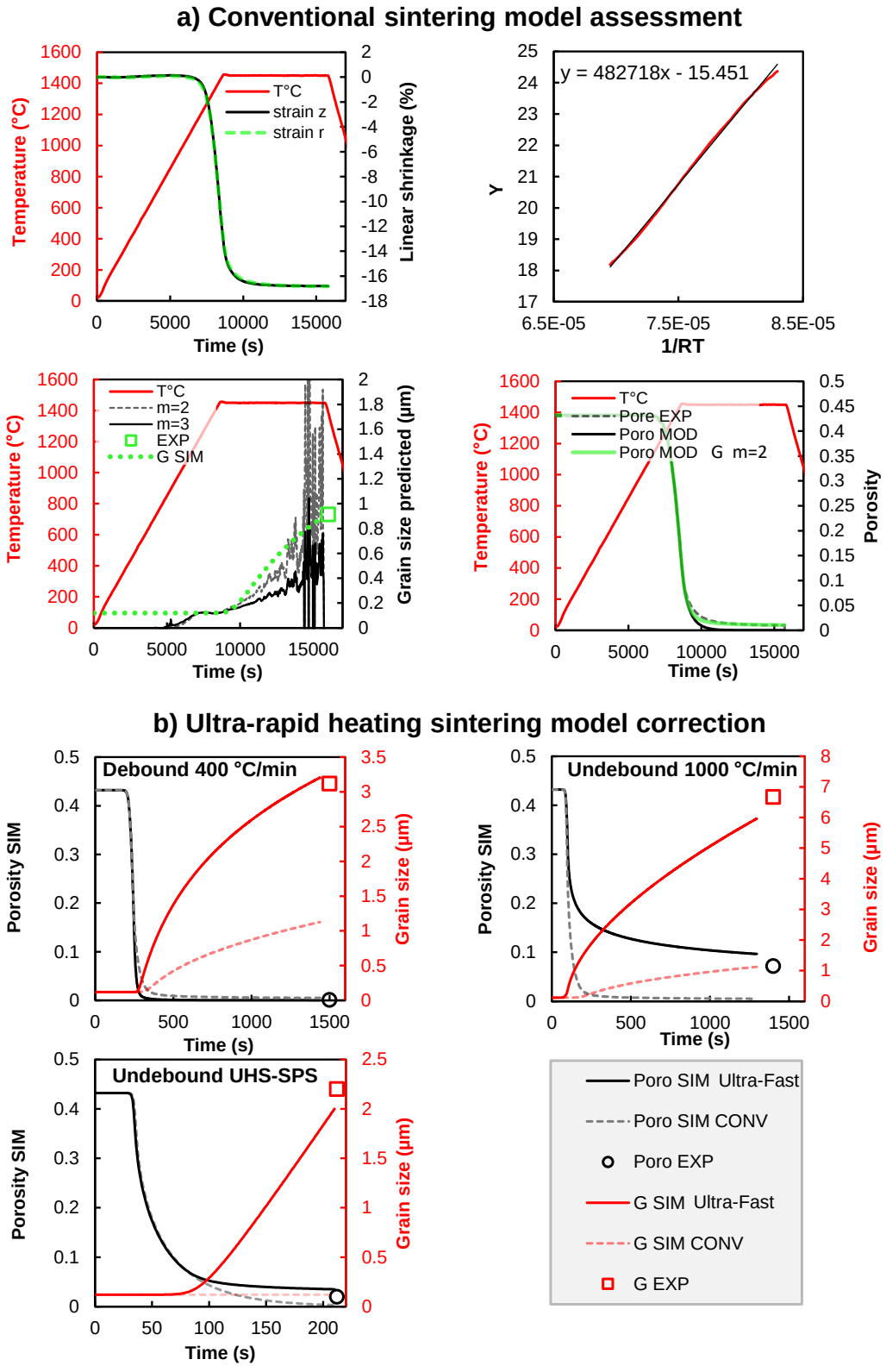

Figure 8 Assessment of the different sintering behavior, (a) conventional debound sample behavior with the dilatometry curves, the sintering model linear regression, the final stage grain growth assessment and the model verification, (b) adaptation of the conventional model parameters "CONV" to "ultra-fast" sintering conditions; "EXP" refers to experimental point and "SIM" to simulation curves.

3.2.5. ETMM simulations or ultra-rapid sintering

Now that the sintering model is identified and adapted to the different ultra-rapid sintering conditions, these parameters can be inserted into the FEM simulation. The ETMM simulation includes the Joule heating of the SPS graphite furnace, the surface-to-surface radiation and the sintering of the sample that is located in the furnace. The simulation of the 1000 °C/min experiment is presented first as it is the fastest-regulated heating test besides UHS. In Figure 9.a, the simulated heating of the SPS furnace is shown, and a zoom inset is made to represent the sample. In the latter, the simulated sintering shrinkage is shown with the initial shape represented by the black lines. Different virtual temperature probes are used to measure the maximum temperature of the heating element which has the highest temperature of the whole SPS column, and the specimen's minimum, maximum, and average temperature. The specimen's min-max temperature difference is also calculated. All these probe temperatures are plotted in Figure 9.b. It shows that at the end of the heating, the furnace heating element is at a maximum temperature close to 2000°C. The set sample temperature of 1600°C is well respected with 30 s overshot at the beginning of the dwell. The sample temperature difference in the dwell is low and of about 40 °C. The maximum sample temperature difference is during the heating with 150 °C. It is the most critical moment where the developed stress can overcome the strength of the specimen creating cracks and failure of the sample. As shown, the heating of the sample from the side makes the upper part of the sample the hottest. The relative density, grain size curves and the corresponding simulated specimen fields are reported in Figure 9.f,c and d. This shows the upper part of the sample with the higher temperature as higher relative density and grain size. The maximum porosity difference is 3% and the grain size difference is 2 µm. This small difference can be explained by the short sintering time and the low-temperature difference in the sample. The temperature gradients cause dissimilar densification rates and significant stress development in the part. The ETMM simulation also helps visualize the developed stress within the sample. In figure 9.e, the von Mises stress field of the sample is represented at the end of the heating where the sample deformation is maximum (where the part is most likely to break). This shows that at this time, the sintering has a slight advance on the top of the specimen where the heating is higher.

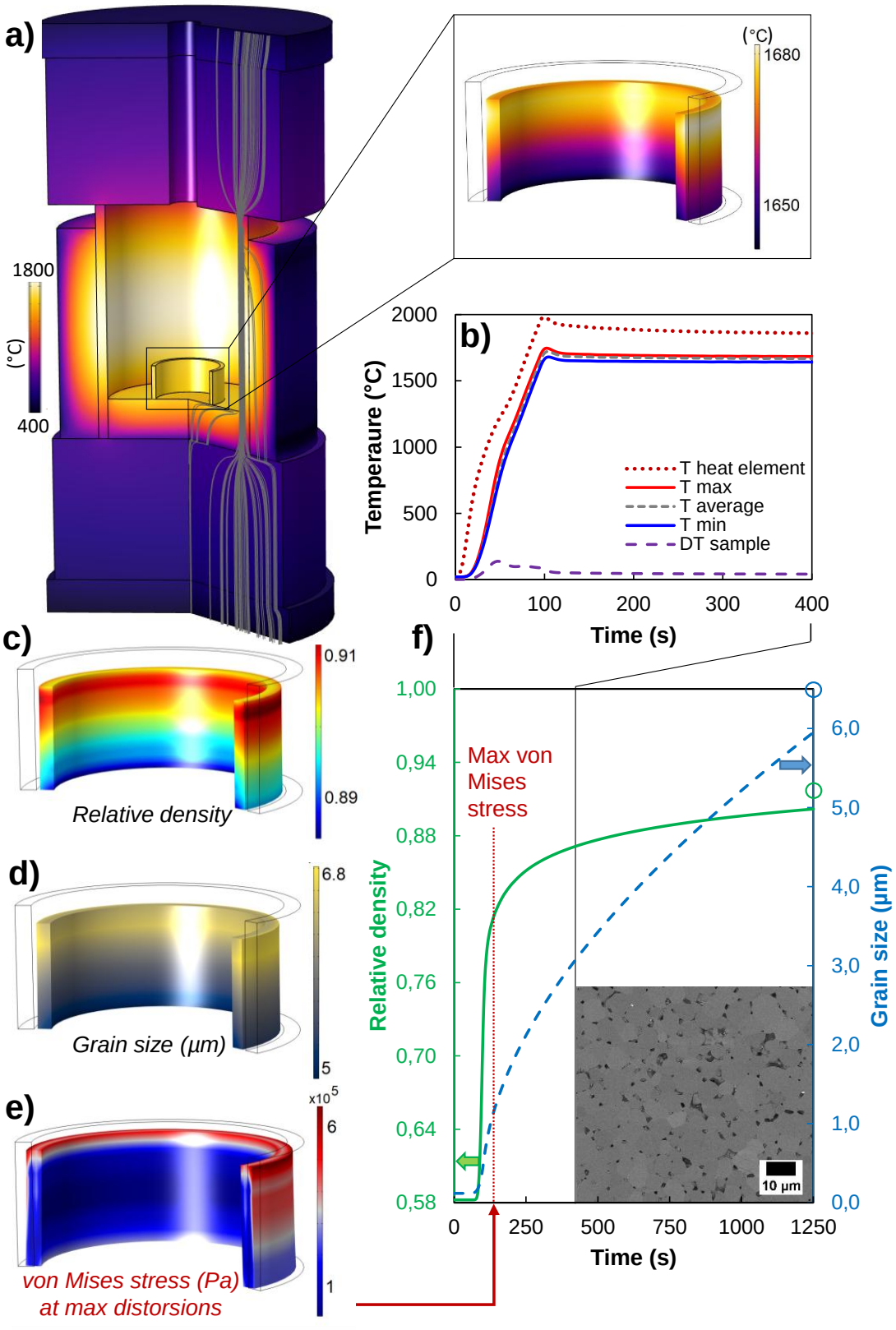

Figure 9. Electro-thermal-mechanical-microstructural simulation: (a) Simulated heating of the SPS column and zoom of the sample, (b) Temperature probes of the column and sample, (c) relative density, (d) grain size, (e) von Mises stress, (f) simulated relative density and grain size curves.

In Figure 10, the ETMM simulation of the fastest heating-rate tests without cracks are compared with in Figure 10.a the 400 °C/min test for the debound sample and in Figure 10.b the 1000 °C/min test corresponding to undebound specimen. For each of these tests, the simulated specimen fields of the temperature, relative density, and grain size at the end of sintering are presented. The von Mises stress field is also presented at the end of the heating to visualize the specimen at highest deformation. For the 400 °C/min debound test, less deformation, lower porosity and a smaller grain size are observed. The fact that the grain size is smaller despite the lower heating rate and porosity for debound case suggests the organics and the *in situ* debinding enhance the grain growth while maintaining a certain level of porosity by the carbo-thermal reduction [43]. The other aspect is the recorded curve of the maximum von Mises stress in specimens. As expected, it shows the highest values during the heating and a rapid decrease and stabilization during the dwell. The highest von Mises stress occurs above 1000 °C. In Figure 1, the residual carbon is fully formed at 450 °C; however, given the extreme heating rate, it is possible that the decomposition is shifted toward the maximum von Mises temperature. Since Dolapix CE64 is endothermic, it can compensate for the surface overheating caused by radiation. A shift in the decomposition of organics may also induce a slight shrinkage, which helps relax internal stresses during this critical heating stage. It is interesting to note that the highest value is close to a few MPa. As these two tests are crack-free critical heating rate, this suggests that stress values up to 2 MPa do not involve failure of the specimen. If the simulated stress under certain conditions is above this value, it can be considered a potential failure condition.

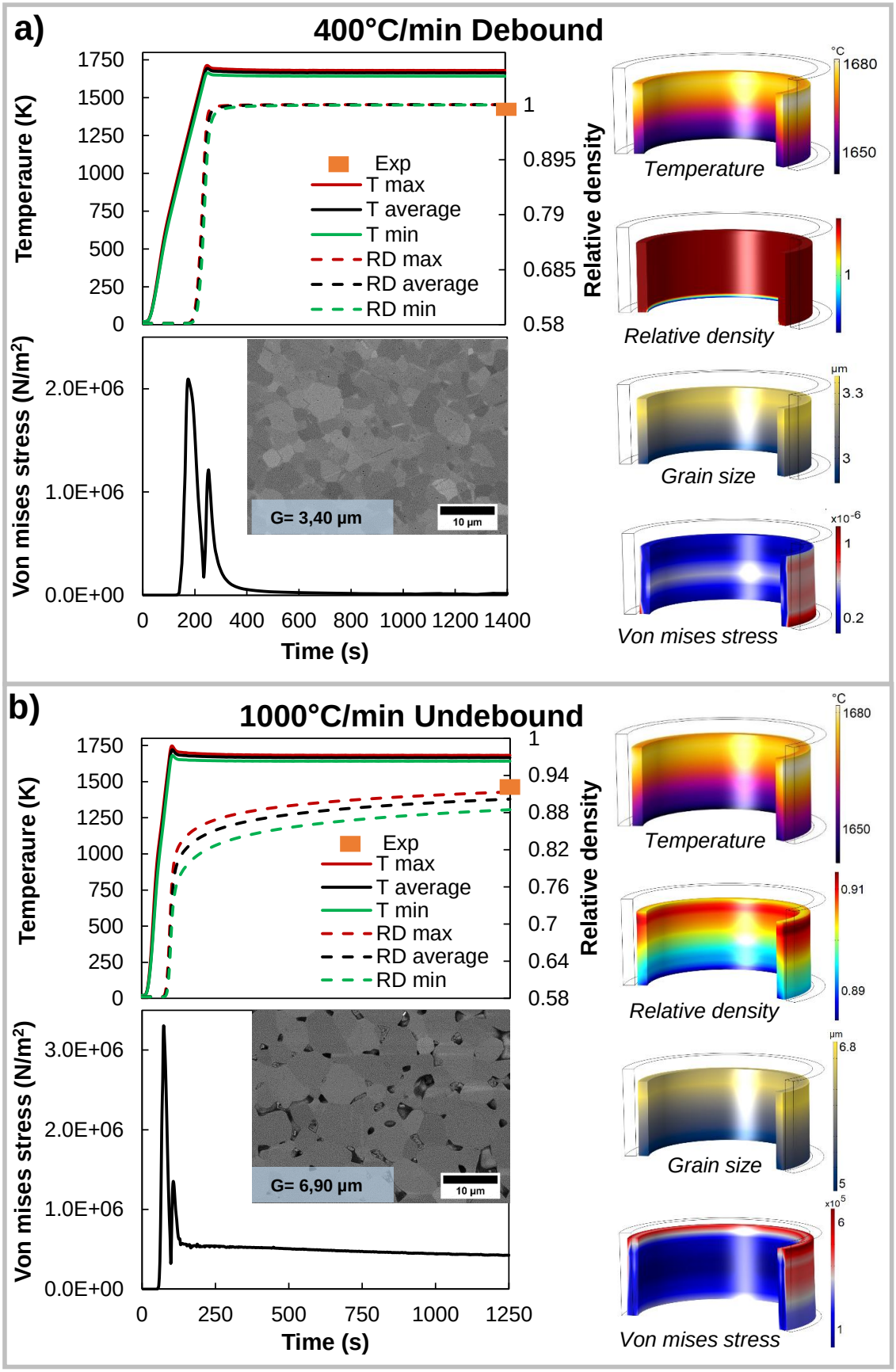

Figure 10: ETMM simulation of fastest heating-rate tests without cracks: (a) 400°C/min debound sample and (b) 1000)C/min undebound sample

3.2.6. Stress analysis and critical heating rate and wall thickness criteria

The histogram (Figure 11) compares the maximum simulated von Mises stress developed in the sample during the cycle with each critical crack-free heating rate (50 °C/min, 200 °C/min, 400 °C/min, and 1000 °C/min). One key observation is that debound specimens exhibit lower stress levels than undebound ones. This suggests that the porous skeleton in undebound samples, despite their inherent fragility, can tolerate higher stresses than the debound parts. As previously discussed, debinding at 600 °C appears to promote particle consolidation, which in turn increases the fragility of the debound parts. Consequently, undebound samples demonstrate behavior that is more tolerant during ultra-fast heating and can withstand stresses of up to 3 MPa, enabling crack-free sintering under the extreme heating rates of UHS.

Part geometry and wall thickness also play a critical role in heating homogeneity and the resulting stress distribution. Thicker samples experience greater thermal gradients, which lead to higher internal stresses and limit the maximum achievable heating rate. At extreme heating rates, such as those used in UHS, only undebound samples with low wall thickness (~1 mm) can be sintered without cracking. Therefore, sample geometry is a crucial factor for successful UHS sintering. For example, hollow cylinders benefit from highly favorable radiation exposure. In the following section, various complex shapes with unfavorable radiation conditions are examined to evaluate the UHS-SPS process's ability to sinter intricate geometries.

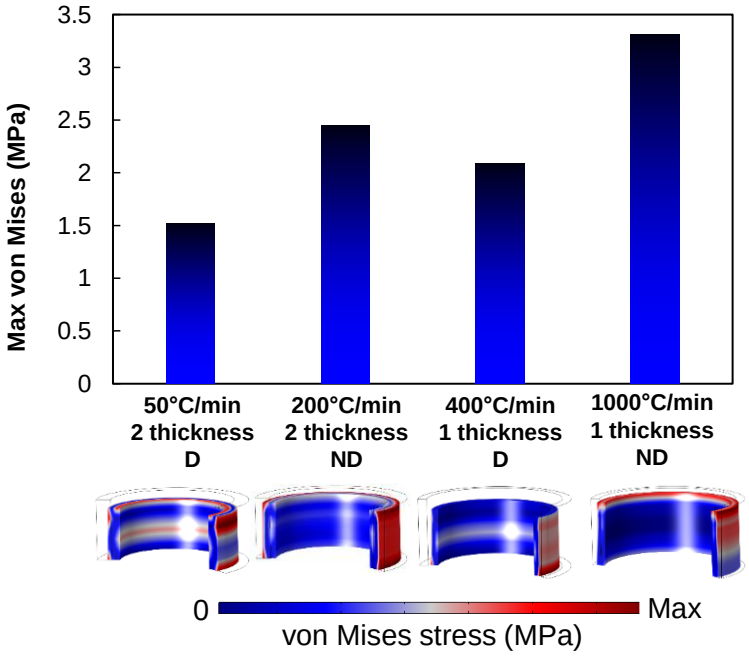

Figure 11: Histogram and simulation of maximum von Mises stress for the critical heating rate (above which cracks appear)

3.3. UHS-SPS of complex shapes

In this experimental section, UHS-SPS is applied to different large-sized complex shapes to test the feasibility of scalable UHS-SPS on different shapes. As suggested by the heating rate study, only undebound and thin-walled thickness samples were tested to focus the investigation on the impact of geometry on the success of UHS-SPS. Two impeller geometries are tested one with 5 blades which has the largest diameter of 30 mm. A more complex impeller with 7 blades, a 10° building angle and a conical base is also tested to investigate a more challenging radiation exposure. Both samples have a 5 mm height and are first tested in 1000 °C/min (ultra-rapid conditions) and for the extreme UHS-SPS conditions which have an average heating rate close to 3600°C (with local maximum heating rate of >10 000°C/min). The results are reported in figure 12. All the shapes have been successfully sintered from ultra-rapid to UHS-SPS conditions without cracks. The initial shape is well preserved; the 5-blade impeller shows only a slight warping at the base. For the 7-blade impeller, we observe only a small detachment of the printing beads from the blades. The latter are already partially detached in the printed part (see green section), but this effect seems slightly more pronounced for UHS-SPS. This suggests a temperature difference between the external layers, which are more exposed to thermal radiation, and the internal layers.

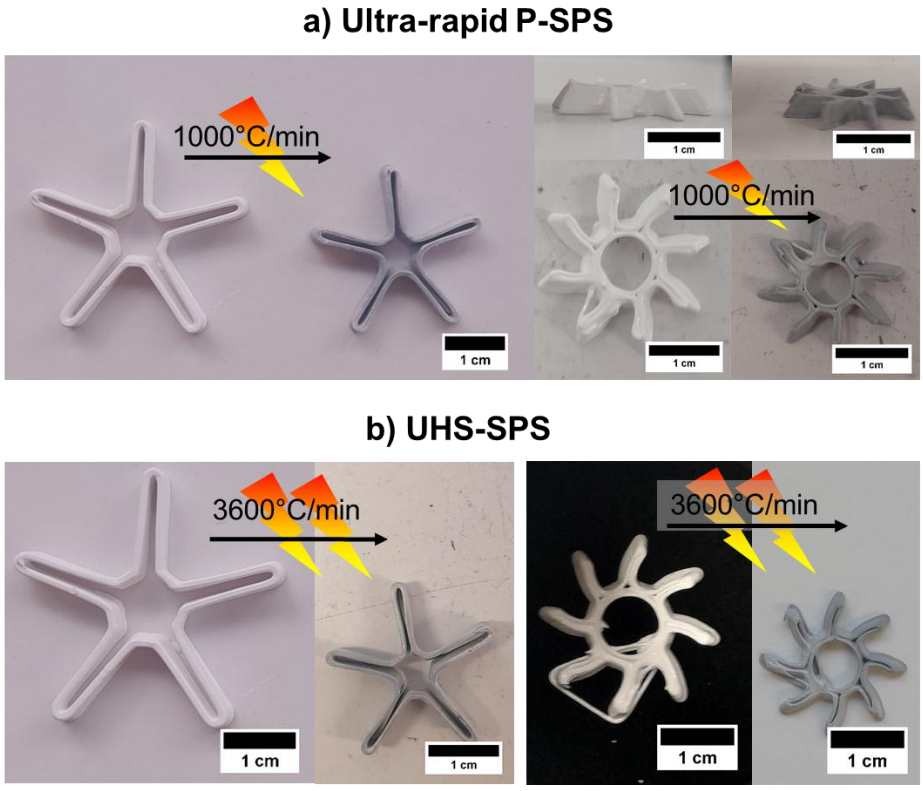

Figure 12. (a) Ultra-rapid P-SPS 1000°C/min sintering and (b) UHS-SPS 3600°C/min sintering

The previous impeller was large but with only 5 mm height which makes it relatively favorable for homogeneous thermal radiation from the heating element. Figure 13 shows the case of a 10 mm height 7 blades shapes in UHS-SPS. This tall impeller version is a more sensitive configuration for thermal radiation. The simulation tool is particularly well suited here to investigate this case where failure happens in one half of the sample. In figure 13.a, we first observe the green impeller and the results after the UHS-SPS process. As indicated by the red arrows, cracks appear on the conical base and propagate between the blades; a slight deformation of the parts is noticeable. The heating simulation, represented in the SPS column, shows that the heat is most concentrated in the heating element (at mid-height) and radiates onto the sample. However, the zoomed-in view of the sample reveals that the temperature distribution is not homogeneous, with the highest temperature observed at the tips of the blades that are more exposed to radiation. The sample also appears to be primarily heated from above by the heating element. The final impeller shrinkage simulated has limited warping but this simulation assumes no cracks. In order to investigate the cause of the specimen failure, we must determine the most probable moment of crack appearance time and examine the physical fields at this precise time.

Figure 13.b explores the thermomechanical behavior at the critical sintering stage where cracks are expected to happen to occur. In order to detect the time at which the developed thermal gradients and stress generate cracks, a graph is plotted with the curves of PID regulated temperature, sample's maximum temperature difference (△T) and maximum von Mises stress. A significant peak around 20 seconds is observed in both the temperature gradient and von Mises stress. The von Mises stress in this area reaches a value of 100 MPa, which is well above the 3 MPa determined during the sintering of cylinder parts at 1000 °C/min. At that time, different physical parameters are compared. To analyze the primary origin of the failure, the surface-to-surface radiation exchanges are analyzed. The radiosity (J) of the chamber is reported to detect the maximum emitting area, which is here the mid-height of the graphite-heating element. The impeller surface discloses the incoming irradiated flux (G). This shown that the cone base and the interior surfaces of the impeller blades are nearly not exposed to radiation compared to the tip of the blades. This is confirmed by the temperature distribution in the impeller that has a 500 °C temperature difference between the cone (less heated) and the blades tip. This difference generates high stress inside the impeller. The developed stress is very high in the internal part of the cone. A notable variation in relative density is also observed between the inner cone surface (58%) and the blade tip (97%). If we observe the main crack in Figure 13.a, it seems to start from the cone which as the stress above the 3 MPa previously determined and propagate into the adjacent blades. This case shows the link between radiation exposure heterogeneities and the resulting gradients that can lead to part failure, which is not solely dependent on scale.

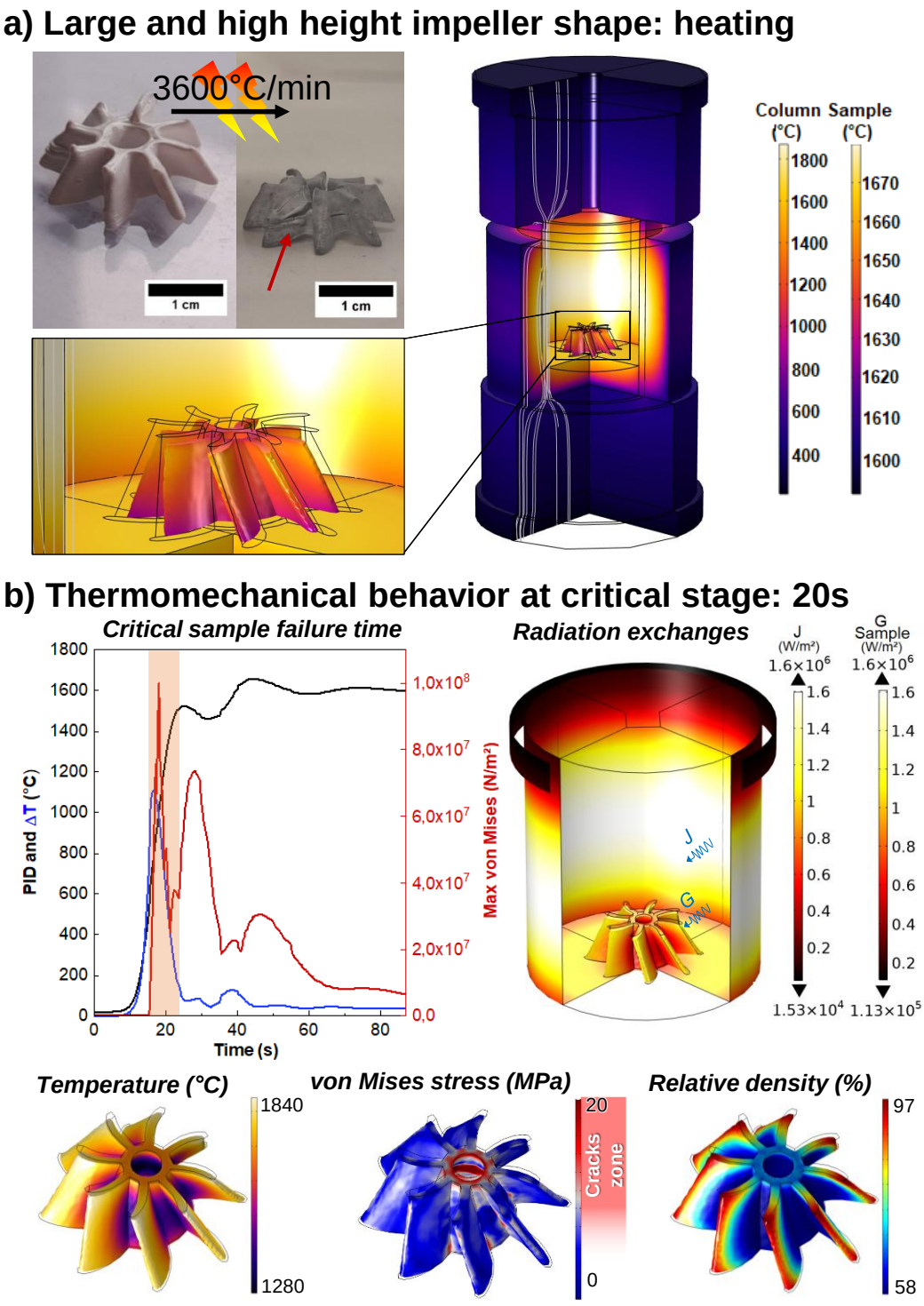

Figure 13: Simulation of 10 mm height impeller: (a) Results of impeller sintered and heating simulation of SPS column and sample and (b) PID, ΔT and max von Mises stress curves simulated radiation exchanges between the column and the sample, and simulated temperature, von Mises stress and relative density of the sample at the critical stage (20s)

4. Conclusion

This work provides new insights into the potential for developing a scalable ultrafast-high-temperature-sintering (UHS) process. UHS has shown great promise for sintering small, thin-walled, and complex-shaped parts in a few seconds. The P-SPS configuration employed in this study, operating under UHS conditions with a heating rate of 3600 °C/min, was validated by comparing the microstructure of a 10 mm lattice structure with the one obtained using conventional UHS methods. The similarity of the resulting microstructures and micro-harness confirms that UHS-SPS does not degrade the properties compared to the original method, which is difficult to scale. An initial scalability study was conducted by determining the critical wall thickness and optimal heating rate for large printed tubes in the UHS-SPS configuration. It was demonstrated that 10 mm-height tubes with a 20 mm diameter and a wall thickness of 1.3 mm could be sintered without cracks at a heating rate of 1000 °C/min if they are undebound.

The true scalability challenge arises in the UHS-SPS sintering of more complex parts, such as a 30 mm diameter complex impeller with five blades and a more intricate impeller featuring seven angled blades. Both were successfully sintered without cracks at heating rates of 1000 °C/min and 3600 °C/min, demonstrating the robustness and versatility of the UHS-SPS configuration. Only the tall, intricate impeller failed due to parts being less exposed to thermal radiation.

The study also incorporated sintering modeling of the UHS-SPS. It showed that dilatometry-based conventional models can reproduce the ultrafast densification rate. However, adjustments are necessary to accurately capture the final stage sintering and grain growth behavior, which is significantly influenced by carbothermal reduction originating from the carbon contamination. Additionally, finite element method (FEM) simulations were employed to assess the effects of thermal radiation exposure on complex parts, resulting gradients, and the outcome on the sintering. These simulations revealed that homogeneous radiation is difficult to achieve in intricate geometries, resulting in pronounced thermal gradients. Such gradients contribute to the development of internal stresses, which in turn promote deformation and cracking.

This case shows the high impact of shape complexity on radiation exposure heterogeneity, which has an impact as significant as the shape’s dimensions. The thermomechanical simulation tool can be highly valuable for redesigning the shape or optimizing the heating configuration. These results evidence the feasibility of UHS scalability and pave the way for new ultrafast production processes coupling 3D printing and ultrafast sintering.

5. Nomenclature

θ Porosity

$\dot{\theta}$ Porosity elimination rate (s^{-1})

$\underline{\sigma}$ Stress tensor ($N.m^{-2}$)

$\underline{\dot{\varepsilon}}$ Strain rate tensor (s^{-1})

$\dot{\varepsilon}_{eq}$ Equivalent strain rate (s^{-1})

η Viscosity (Pa.s)

η_0 Viscosity pre-exponential factor (Pa.s)

m Creep law grain size sensibility exponent

Q Sintering activation energy ($J.mol^{-1}$)

R Gas constant 8.314 ($J.mol^{-1}.K^{-1}$)

T Temperature (K)

φ Shear modulus

ψ Bulk modulus

P_l Sintering stress (Pa)

$\mathbb{i}$ Identity tensor

$\dot{G}$ Grain growth rate ($m.s^{-1}$)

G Grain size (m)

G_0 Initial grain size (m)

r_0 Initial particle size (m)

p Grain growth equation grain size exponent

n Grain growth porosity function exponent

k_0 Grain growth pre-exponential factor ($m^{1+p}.s^{-1}$)

Q_G Grain growth activation energy ($J.mol^{-1}$)

θ_c Grain growth porosity function critical porosity

$\vec{J}$ Electric current density ($A\ m^{-2}$)

$\vec{E}$ Electric field ($V\ m^{-1}$)

$\boldsymbol{J}$ Electric current density norm ($A\ m^{-2}$)

$\boldsymbol{E}$ Electric field norm ($V\ m^{-1}$)

σ_{elec} Electric conductivity ($S\ m^{-1}$)

ρ Volumetric mass ($kg\ m^{-3}$)

C_p Heat capacity ($J\ kg^{-1}\ K^{-1}$))

T Temperature (K)

κ Thermal conductivity ($W\ m^{-1}\ K^{-1}$)

φ_{csw} Convective heat flux ($W{\cdot}m^{-2}$)

σ_s Stefan Boltzmann constant (5.67.×10^{-8} W·m^{-2}K^{-4})

ϵ Emissivity

T_{water} Water cooling temperature (K)

h_{iw} Surface conductivity (W·m^{-2}·K^{-1})

J Surface radiosity (W·m^{-2})

$\boldsymbol{G}$ Irradiation flux (W·m^{-2})

$\boldsymbol{n}$ Refractive index

$e_b(T)$ Surface radiation produced (W·m^{-2})

ρ_r Reflectivity

φ_{rss} Net inward radiative heat flux (W·m^{-2})

UHS Ultrafast High temperature Sintering

SPS Spark Plasma Sintering

P-SPS Pressureless-SPS

ETMM Electro-Thermal-Mechanical-Microstructural

FEM Finite Element Method

6. Appendix: FEM simulation of the P-SPS, thermomechanical aspect of sintering.

6.1. Electro-Thermal-Mechanical-Microstructural model (ETMM)

6.1.1. Electro-thermal model

The ETMM simulation of pressureless-spark-plasma-sintering gathers a Joule heating/radiative model coupled to a sintering model. The Joule heating part has two main equations for the charge conservation and heat transfer.

$$\nabla.\vec{J} = \nabla.\left(\sigma_{elec}\vec{E}\right) = 0 \quad (1)$$

$$\nabla.\left(-\kappa\nabla T\right) + \rho C_p \frac{dT}{dt} = \boldsymbol{JE} \quad (2)$$

Where the term $\boldsymbol{JE}$ is the volumetric electrical power dissipated.

Concerning the SPS water cooling boundary condition, it is modeled by a convective boundary conditions below, with, h_{iw} the convective coefficient of 600 W·m^{-2}·K^{-1}, T_{water}=300 K.

$$\varphi_{csw} = h_{iw}(T_{water} - T) \quad (3)$$

For the internal solid/vacuum interfaces surface-to-surface thermal radiation is modeled with the radiosity (*J*) equation below that relates incoming thermal irradiation (***G***) and the emitted radiation ($e_b(T)$).

$$J = \rho_r \boldsymbol{G} + \epsilon e_b(T) = \rho_r \boldsymbol{G} + \epsilon \boldsymbol{n}^2 \sigma_s T^4 \quad (4)$$

With the relationship the reflectivity and emissivity:

$$\epsilon = 1 - \rho_r \quad (5)$$

the net inward radiative heat flux φ_{rss} can be calculated as:

$$\varphi_{rss} = \epsilon(\boldsymbol{G} - e_b(T)) \quad (6).$$

In the simulations the emissivity of graphite and alumina is 0.8 and 0.65 for the steel electrode. The evolution of the alumina thermal properties with the porosity have been taken into account by multiply the volumetric mass by the relative density and by using the effective medium approximation corrective factor (1-1.5Θ) for the thermal conductivity. The graphite electro-thermal properties are detailed in ref [54]

6.1.2. Pressureless sintering model

The sintering part utilizes the continuum theory of sintering which is based here on the Skorohod-Olevsky model [42]. The first part is the momentum equation.

$$\nabla.\underline{\sigma} = 0 \quad (7)$$

The Skorohod-Olevsky model behavior of sintering relates the strain rate and stress tensors and sintering behavior which is as below for the case of pressureless sintering.

$$\underline{\sigma} = 2\eta\left(\varphi\underline{\dot{\varepsilon}} + \left(\psi - \frac{1}{3}\varphi\right)tr\left(\underline{\dot{\varepsilon}}\right)\mathbb{1}\right) + Pl\mathbb{1} \quad (8)$$

The shear φ and bulk ψ moduli are porosity functions that have been previously determined for the BMA15 alumina. Their expressions are below.

$$\varphi = \left(1 - \frac{\theta}{0.6}\right)^{3.9} \quad (9)$$

$$\psi = 0.87\frac{(0.51-\theta)^{2.2}}{\theta} \quad (10)$$

The diffusional viscosity expression and their grain size sensitivity is expressed as below.

$$2\eta = \left(\frac{G}{G_0}\right)^m \eta_0 T\exp(\frac{Q}{RT}) \quad (11)$$

With m=3 for grain-boundary-diffusion creep and m=2 for lattice-diffusion creep.

The activation energy Q and viscosity pre-exponent constant η_0 are determined by sintering dilatometry using the next regression equation.

$$Y = ln\left(\frac{-3(1-\theta)^3}{r_0 T\dot{\theta}\psi}\right) = ln\left(\frac{\eta_0}{\alpha}\right) + \frac{Q}{RT} \quad (12)$$

The mass conservation equation is used to relate the volume change rate and the porosity elimination rate.

$$\frac{\dot{\theta}}{(1-\theta)} = \dot{\varepsilon}_x + \dot{\varepsilon}_y + \dot{\varepsilon}_z \quad (13)$$

The grain growth with porosity influence is modeled by the following equation.

$$\dot{G} = \frac{k_0}{G^p}\left(\frac{\theta_c}{\theta+\theta_c}\right)^n exp\left(\frac{-Q_G}{RT}\right) \quad (14)$$

During the final stage of sintering, grain growth becomes particularly pronounced and can significantly affect the densification kinetics. Using the pressureless sintering model, the evolution of grain size can be inferred from the porosity data at this stage through the following relationship.

$$G = \left(\frac{-\frac{6\alpha G_0^m}{\eta_0}\exp(\frac{-Q}{RT})}{\dot{\theta}T}\frac{(1-\theta)^3}{\psi}\right)^{\frac{1}{m+1}} \quad (15).$$

This equation should be applied only after determining the relevant sintering parameters. Since the specific sintering mechanism and its associated grain growth exponent 'm' are not yet identified, multiple grain size trajectories can be generated depending on the assumed mechanism. Agglomeration often maintains a constant initial particle radius (r_0), the equation can then be reformulated as follows.

$$G = \left(\frac{-3(1-\theta)^3 G_0^m}{\dot{\theta} r_0 \frac{\eta_0}{\alpha} T\exp(\frac{Q}{RT})\psi}\right)^{\frac{1}{m}} \quad (16)$$

6.2. Key thermal and physical properties of materials and heating elements

Table A: Temperature dependent material properties of graphite, electrodes [54], graphite felt [35] and alumina [55] (with 'θ' for the alumina porosity).

Materials		Expression
Graphite	*Cp* (J.kg^{-1}.K^{-1})	34.3+2.72.T-9.6E-4.T^2
Electrode		446.5+0.162.T
Graphite felt		$34.3 + 2.72\,T - 9.6\,10^{-4}\,T^2$
Alumina		850
Graphite	*κ* (W.m^{-1}.K^{-1})	123-6.99E-2.T+1.55E-5.T^2
Electrode		9.99+0.0175.T
Graphite felt		$0.019\,e^{0.0015\,T}$
Alumina		(39500.T$^{-1.26}$).(1-1.5θ)
Graphite	*ρ* (kg.m^{-3})	1904-0.0141.T
Electrode		7900
Graphite felt		200
Alumina		(3899).(1- θ)
Graphite	σ_{elec} (S/m)	1/[1.70E-5-1.87E-8.T+1.26E-11.T^2-2.46E-15.T^3]
Electrode		1/[(50.2+0.0838.T-1.76E-5.T^2).1E-8]
Graphite felt		$415\,\ln(T) - 2367$
Alumina		(1/(8.7E19T$^{-4.82}$)).(1-1.5θ)
Graphite	*ϵ*	0.8
Electrode		0.6
Graphite felt		0.9
Alumina		0.8

Acknowledgements

The PhD of Flavie Lebas was funded by the University of Caen Normandy. The help and support of Jérôme Lecourt and Christelle Bilot is gratefully acknowledged.

Declaration of competing interest

The authors declare that they have no known competing financial interests or personal relationships that could have appeared to influence the work reported in this paper.

References

[1] M. Cologna, B. Rashkova, R. Raj, Flash Sintering of Nanograin Zirconia in <5 s at 850°C, J. Am. Ceram. Soc. 93 (2010) 3556–3559. https://doi.org/10.1111/j.1551-2916.2010.04089.x.

[2] L. Porz, M. Scherer, D. Huhn, L.-M. Heine, S. Britten, L. Rebohle, M. Neubert, M. Brown, P. Lascelles, R. Kitson, D. Rettenwander, L. Fulanovic, E. Bruder, P. Breckner, D. Isaia, T. Frömling, J. Rödel, W. Rheinheimer, Blacklight sintering of ceramics, Mater. Horiz. 9 (2022) 1717–1726. https://doi.org/10.1039/D2MH00177B.

[3] K.K. Singh, A.V. Subrahmanyam, Fast Firing of Ceramics—A Review, Trans. Indian Ceram. Soc. 35 (1976) 26–30. https://doi.org/10.1080/0371750X.1976.10840848.

[4] D.E. García, J. Seidel, R. Janssen, N. Claussen, Fast firing of alumina, J. Eur. Ceram. Soc. 15 (1995) 935–938. https://doi.org/10.1016/0955-2219(95)00071-2.

[5] M. Biesuz, E. De Bona, C. Manière, Fast firing of 3 mol% yttria-stabilized zirconia: On the effect of heating rate on sintering, J. Am. Ceram. Soc. 107 (2024) 6596–6606. https://doi.org/10.1111/jace.19989.

[6] S. Grasso, T. Saunders, H. Porwal, B. Milsom, A. Tudball, M. Reece, Flash Spark Plasma Sintering (FSPS) of α and β SiC, J. Am. Ceram. Soc. 99 (2016) 1534–1543. https://doi.org/10.1111/jace.14158.

[7] C. Manière, G. Lee, E.A. Olevsky, All-Materials-Inclusive Flash Spark Plasma Sintering, Sci. Rep. 7 (2017) 15071. https://doi.org/10.1038/s41598-017-15365-x.

[8] Yu.V. Bykov, S.V. Egorov, A.G. Eremeev, I.V. Plotnikov, K.I. Rybakov, A.A. Sorokin, V.V. Kholoptsev, Flash Sintering of Oxide Ceramics under Microwave Heating, Tech. Phys. 63 (2018) 391–397. https://doi.org/10.1134/S1063784218030052.

[9] G. Riquet, T. Grippi, C. Harnois, S. Marinel, C. Manière, Flash microwave sintering of zirconia by multiple susceptors cascade strategy, J. Eur. Ceram. Soc. 43 (2023) 4896–4905. https://doi.org/10.1016/j.jeurceramsoc.2023.04.004.

[10] M. Biesuz, V.M. Sglavo, Flash sintering of ceramics, J. Eur. Ceram. Soc. 39 (2019) 115–143. https://doi.org/10.1016/j.jeurceramsoc.2018.08.048.

[11] F.C. Nunes, P.A. Lançoni, G.H.M. Gomes, K.F. Santos, E.Y. Nagata, J.V. Campos, I.C.F. Moraes, J.K.M.B. Daguano, E.M.J.A. Pallone, Flash sintering of 3D-printed 3YSZ scaffolds for bone tissue engineering, Ceram. Int. 51 (2025) 17704–17717. https://doi.org/10.1016/j.ceramint.2025.01.541.

[12] F.C. Nunes, G.H.M. Gomes, J.V. Campos, J.K.M.B. Daguano, E.M.J.A. Pallone, Influence of controlled current ramp on flash sintering of 3D-printed zirconia scaffolds, Mater. Lett. 398 (2025) 138934. https://doi.org/10.1016/j.matlet.2025.138934.

[13] C. Wang, W. Ping, Q. Bai, H. Cui, R. Hensleigh, R. Wang, A.H. Brozena, Z. Xu, J. Dai, Y. Pei, C. Zheng, G. Pastel, J. Gao, X. Wang, H. Wang, J.-C. Zhao, B. Yang, X. (Rayne) Zheng, J. Luo, Y. Mo, B. Dunn, L. Hu, A general method to synthesize and sinter bulk ceramics in seconds, Science 368 (2020) 521–526. https://doi.org/10.1126/science.aaz7681.

[14] M. Kermani, D. Zhu, J. Li, J. Wu, Y. Lin, Z. Dai, C. Hu, S. Grasso, Ultra-fast High-temperature Sintering (UHS) of translucent alumina, Open Ceram. 9 (2022) 100202. https://doi.org/10.1016/j.oceram.2021.100202.

[15] R.P. Behera, M.J.-H. Reavley, Z. Du, C.L. Gan, H. Le Ferrand, Ultrafast high-temperature sintering of dense and textured alumina, J. Eur. Ceram. Soc. 42 (2022) 7122–7133. https://doi.org/10.1016/j.jeurceramsoc.2022.08.014.

[16] M. Biesuz, T.H.D. Beauvoir, E. De Bona, M. Cassetta, C. Manière, V.M. Sglavo, C. Estournès, Ultrafast high-temperature sintering (UHS) vs. conventional sintering of 3YSZ: Microstructure and properties, J. Eur. Ceram. Soc. 44 (2024) 4741–4750. https://doi.org/10.1016/j.jeurceramsoc.2024.01.064.

[17] M. Kermani, J. Dong, M. Biesuz, Y. Linx, H. Deng, V.M. Sglavo, M.J. Reece, C. Hu, S. Grasso, Ultrafast high-temperature sintering (UHS) of fine grained α-Al2O3, J. Eur. Ceram. Soc. 41 (2021) 6626–6633. https://doi.org/10.1016/j.jeurceramsoc.2021.05.056.
[18] M.J.-H. Reavley, H. Guo, J. Yuan, A.Y.R. Ng, T.Y.K. Ho, H.T. Tan, Z. Du, C.L. Gan, Ultrafast high-temperature sintering of barium titanate ceramics with colossal dielectric constants, J. Eur. Ceram. Soc. 42 (2022) 4934–4943. https://doi.org/10.1016/j.jeurceramsoc.2022.04.056.
[19] T.P. Mishra, S. Wang, C. Lenser, D. Jennings, M. Kindelmann, W. Rheinheimer, C. Broeckmann, M. Bram, O. Guillon, Ultra-fast high-temperature sintering of strontium titanate, Acta Mater. 231 (2022) 117918. https://doi.org/10.1016/j.actamat.2022.117918.
[20] E. De Bona, L. Karacasulu, C. Vakifahmetoglu, V.M. Sglavo, M. Biesuz, Ultrafast high-temperature sintering (UHS) of WC and WC-containing ZrB2, J. Alloys Compd. 986 (2024) 174102. https://doi.org/10.1016/j.jallcom.2024.174102.
[21] E. De Bona, C. Manière, V.M. Sglavo, M. Biesuz, Ultrafast high-temperature sintering (UHS) of ZrB2-based materials, J. Eur. Ceram. Soc. 44 (2024) 567–573. https://doi.org/10.1016/j.jeurceramsoc.2023.09.007.
[22] F. Zuo, Q. Wang, Z.-Q. Yan, M. Kermani, S. Grasso, G.-L. Nie, B.-B. Jiang, F.-P. He, H.-T. Lin, L.-G. Wang, Upscaling Ultrafast High-Temperature Sintering (UHS) to consolidate large-sized and complex-shaped ceramics, Scr. Mater. 221 (2022) 114973. https://doi.org/10.1016/j.scriptamat.2022.114973.
[23] R. Yamanoglu, Pressureless Spark Plasma Sintering: A Perspective from Conventional Sintering to Accelerated Sintering Without Pressure, Powder Metall. Met. Ceram. 57 (2019) 513–525. https://doi.org/10.1007/s11106-019-00010-1.
[24] R. Yamanoglu, N. Gulsoy, E.A. Olevsky, H.O. Gulsoy, Production of porous Ti5Al2.5Fe alloy via pressureless spark plasma sintering, J. Alloys Compd. 680 (2016) 654–658. https://doi.org/10.1016/j.jallcom.2016.04.176.
[25] Y. Quan, F. Zhang, H. Rebl, B. Nebe, O. Keßler, E. Burkel, Ti6Al4V foams fabricated by spark plasma sintering with post-heat treatment, Mater. Sci. Eng. A 565 (2013) 118–125. https://doi.org/10.1016/j.msea.2012.12.026.
[26] D. Salamon, Z. Shen, Pressure-less spark plasma sintering of alumina, Mater. Sci. Eng. A 475 (2008) 105–107. https://doi.org/10.1016/j.msea.2007.01.162.
[27] L. Bertolla, I. Dlouhý, P. Tatarko, A. Viani, A. Mahajan, Z. Chlup, M.J. Reece, A.R. Boccaccini, Pressureless spark plasma–sintered Bioglass ® 45S5 with enhanced mechanical properties and stress–induced new phase formation, J. Eur. Ceram. Soc. 37 (2017) 2727–2736. https://doi.org/10.1016/j.jeurceramsoc.2017.02.003.
[28] W.L. Bradbury, E.A. Olevsky, Production of SiC–C composites by free-pressureless spark plasma sintering (FPSPS), Scr. Mater. 63 (2010) 77–80. https://doi.org/10.1016/j.scriptamat.2010.03.009.
[29] D. Giuntini, X. Wei, A.L. Maximenko, L. Wei, A.M. Ilyina, E.A. Olevsky, Initial stage of Free Pressureless Spark-Plasma Sintering of vanadium carbide: Determination of surface diffusion parameters, Int. J. Refract. Met. Hard Mater. 41 (2013) 501–506. https://doi.org/10.1016/j.ijrmhm.2013.06.009.
[30] A.-K. Hofer, A. Kocjan, R. Bermejo, High-strength lithography-based additive manufacturing of ceramic components with rapid sintering, Addit. Manuf. 59 (2022) 103141. https://doi.org/10.1016/j.addma.2022.103141.
[31] E. Peng, D. Zhang, J. Ding, Ceramic Robocasting: Recent Achievements, Potential, and Future Developments, Adv. Mater. 30 (2018) 1802404. https://doi.org/10.1002/adma.201802404.

[32] E. Feilden, E.G.-T. Blanca, F. Giuliani, E. Saiz, L. Vandeperre, Robocasting of structural ceramic parts with hydrogel inks, J. Eur. Ceram. Soc. 36 (2016) 2525–2533. https://doi.org/10.1016/j.jeurceramsoc.2016.03.001.
[33] S. Eqtesadi, A. Motealleh, F.H. Perera, P. Miranda, A. Pajares, R. Wendelbo, F. Guiberteau, A.L. Ortiz, Fabricating geometrically-complex B4C ceramic components by robocasting and pressureless spark plasma sintering, Scr. Mater. 145 (2018) 14–18. https://doi.org/10.1016/j.scriptamat.2017.10.001.
[34] S. Bhandari, O. Hanzel, P. Veteška, M. Janek, E. De Bona, V.M. Sglavo, M. Biesuz, G. Franchin, From rapid prototyping to rapid firing: on the feasibility of high-speed production for complex $BaTiO_3$ components, J. Am. Ceram. Soc. 107 (2024) 6562–6573. https://doi.org/10.1111/jace.19950.
[35] S. Bhandari, C. Manière, F. Sedona, E. De Bona, V.M. Sglavo, P. Colombo, L. Fambri, M. Biesuz, G. Franchin, Ultra-rapid debinding and sintering of additively manufactured ceramics by ultrafast high-temperature sintering, J. Eur. Ceram. Soc. 44 (2024) 328–340. https://doi.org/10.1016/j.jeurceramsoc.2023.08.040.
[36] S. Bhandari, T. Heim, E. De Bona, V.M. Sglavo, W. Rheinheimer, M. Biesuz, G. Franchin, Rapid processing of Al2O3 ceramics by fused filament fabrication and ultrafast high-temperature debinding and sintering, J. Alloys Compd. 1017 (2025) 178812. https://doi.org/10.1016/j.jallcom.2025.178812.
[37] B.P. Singh, R. Menchavez, C. Takai, M. Fuji, M. Takahashi, Stability of dispersions of colloidal alumina particles in aqueous suspensions, J. Colloid Interface Sci. 291 (2005) 181–186. https://doi.org/10.1016/j.jcis.2005.04.091.
[38] F. Lebas, S. Marinel, C. Bilot, R. Herbinet, L. Le Pluart, C. Manière, Versatile aqueous alumina suspensions formulations by one step ball milling for robocasting from fine to coarse powders, Mater. Today Chem. 45 (2025) 102647. https://doi.org/10.1016/j.mtchem.2025.102647.
[39] M. Guo, Q. Dong, H. Xie, C. Wang, Y. Zhao, X. Wang, W. Zhong, Z. Li, R. Wang, Y. Wang, L. Hao, S. He, G. Chen, W. Xiong, J.-C. Zhao, L. Hu, Ultrafast high-temperature sintering to avoid metal loss toward high-performance and scalable cermets, Matter 5 (2022) 594–604. https://doi.org/10.1016/j.matt.2021.11.008.
[40] M.I. Mendelson, Average Grain Size in Polycrystalline Ceramics, J. Am. Ceram. Soc. 52 (1969) 443–446. https://doi.org/10.1111/j.1151-2916.1969.tb11975.x.
[41] C. Manière, C. Harnois, G. Riquet, J. Lecourt, C. Bilot, S. Marinel, Flash spark plasma sintering of zirconia nanoparticles: Electro-thermal-mechanical-microstructural simulation and scalability solutions, J. Eur. Ceram. Soc. 42 (2022) 216–226. https://doi.org/10.1016/j.jeurceramsoc.2021.09.021.
[42] E.A. Olevsky, Theory of sintering: from discrete to continuum, Mater. Sci. Eng. R Rep. 23 (1998) 41–100. https://doi.org/10.1016/S0927-796X(98)00009-6.
[43] S. Bhandari, O. Hanzel, M. Kermani, V.M. Sglavo, M. Biesuz, G. Franchin, Rapid debinding and sintering of alumina ceramics fabricated by direct ink writing, J. Eur. Ceram. Soc. 45 (2025) 117144. https://doi.org/10.1016/j.jeurceramsoc.2024.117144.
[44] A.S.A. Chinelatto, R. Tomasi, Influence of processing atmosphere on the microstructural evolution of submicron alumina powder during sintering, Ceram. Int. 35 (2009) 2915–2920. https://doi.org/10.1016/j.ceramint.2009.03.037.
[45] A.M. Thompson, M.P. Harmer, Influence of Atmosphere on the Final-Stage Sintering Kinetics of Ultra-High-Purity Alumina, J. Am. Ceram. Soc. 76 (1993) 2248–2256. https://doi.org/10.1111/j.1151-2916.1993.tb07761.x.
[46] Z. Guo, R.I. Todd, Acceleration of grain boundary diffusion during ultra-fast firing (UHS) of alumina powder compacts, Acta Mater. 282 (2025) 120471. https://doi.org/10.1016/j.actamat.2024.120471.

[47] C. Manière, C. Harnois, C. Couder, C. Bilot, S. Marinel, Assessment of pressure-assisted sintering models through sinter-forging tests: A case study of alumina incorporating capillarity forces, Ceram. Int. 50 (2024) 26171–26181. https://doi.org/10.1016/j.ceramint.2024.04.358.
[48] J. Wang, R. Raj, Estimate of the Activation Energies for Boundary Diffusion from Rate-Controlled Sintering of Pure Alumina, and Alumina Doped with Zirconia or Titania, J. Am. Ceram. Soc. 73 (1990) 1172–1175. https://doi.org/10.1111/j.1151-2916.1990.tb05175.x.
[49] C. Manière, J.S. Diatta, C. Couder, C. Harnois, S. Marinel, Spark plasma sintering grain growth assessment by densification kinetics analysis, Scr. Mater. 228 (2023) 115346. https://doi.org/10.1016/j.scriptamat.2023.115346.
[50] E.A. Olevsky, C. Garcia-Cardona, W.L. Bradbury, C.D. Haines, D.G. Martin, D. Kapoor, Fundamental Aspects of Spark Plasma Sintering: II. Finite Element Analysis of Scalability, J. Am. Ceram. Soc. 95 (2012) 2414–2422. https://doi.org/10.1111/j.1551-2916.2012.05096.x.
[51] G. Kerbart, C. Manière, C. Harnois, S. Marinel, Predicting final stage sintering grain growth affected by porosity, Appl. Mater. Today 20 (2020) 100759. https://doi.org/10.1016/j.apmt.2020.100759.
[52] M. Michálek, M. Michálková, G. Blugan, J. Kuebler, Effect of carbon contamination on the sintering of alumina ceramics, J. Eur. Ceram. Soc. 38 (2018) 193–199. https://doi.org/10.1016/j.jeurceramsoc.2017.08.011.
[53] R. Marder, P. Ghosh, I. Reimanis, W.D. Kaplan, The influence of carbon on the microstructure and wear resistance of alumina, J. Am. Ceram. Soc. 104 (2021) 4214–4225. https://doi.org/10.1111/jace.17832.
[54] C. Manière, C. Harnois, S. Marinel, Role of microstructure reactivity and surface diffusion in explaining flash (ultra-rapid) sintering kinetics, J. Eur. Ceram. Soc. 43 (2023) 2057–2068. https://doi.org/10.1016/j.jeurceramsoc.2022.12.006.
[55] G. Molénat, L. Durand, J. Galy, A. Couret, Temperature Control in Spark Plasma Sintering: An FEM Approach, J. Metall. 2010 (2010) 1–9. https://doi.org/10.1155/2010/145431.